

## Contamination of planktonic food webs in the Mediterranean Sea: Setting the frame for the MERITE-HIPPOCAMPE oceanographic cruise (spring 2019)

Tedetti Marc <sup>1,\*</sup>, Tronczynski Jacek <sup>2</sup>, Carlotti François <sup>1</sup>, Pagano Marc <sup>1</sup>, Ismail Sana Ben <sup>3</sup>, Sammari Cherif <sup>3</sup>, Hassen Malika Bel <sup>3</sup>, Desboeufs Karine <sup>4</sup>, Poindron Charlotte <sup>4</sup>, Chifflet Sandrine <sup>1</sup>, Zouari Amel Bellaaj <sup>3</sup>, Abdennadher Moufida <sup>3</sup>, Amri Sirine <sup>3</sup>, Bănaru Daniela <sup>1</sup>, Abdallah Lotfi Ben <sup>3</sup>, Bhairy Nagib <sup>1</sup>, Boudriga Ismail <sup>3</sup>, Bourin Aude <sup>3</sup>, Brach-Papa Christophe <sup>6</sup>, Briant Nicolas <sup>2</sup>, Cabrol Léa <sup>1</sup>, Chevalier Cristele <sup>1</sup>, Chouba Lassaad <sup>3</sup>, Coudray Sylvain <sup>6</sup>, Yahia Mohamed Nejib Daly <sup>7</sup>, De Garidel-Thoron Thibault <sup>8</sup>, Dufour Aurélie <sup>1</sup>, Dutay Jean-Claude <sup>9</sup>, Espinasse Boris <sup>10</sup>, Fierro-González Pamela <sup>1</sup>, Fournier Michel <sup>1</sup>, Garcia Nicole <sup>1</sup>, Giner Franck <sup>11</sup>, Guigue Catherine <sup>1</sup>, Guilloux Loïc <sup>1</sup>, Hamza Asma <sup>3</sup>, Heimbürger-Boavida Lars-Eric <sup>1</sup>, Jacquet Stéphanie <sup>1</sup>, Knoery Joël <sup>2</sup>, Lajnef Rim <sup>3</sup>, Belkahia Nouha Makhoulouf <sup>12,13</sup>, Malengros Deny <sup>1</sup>, Martinot Pauline L. <sup>1</sup>, Bosse Anthony <sup>1</sup>, Mazur Jean-Charles <sup>8</sup>, Meddeb Marouan <sup>13,14</sup>, Misson Benjamin <sup>15</sup>, Pringault Olivier <sup>1</sup>, Quéméneur Marianne <sup>1</sup>, Radakovitch Olivier <sup>8,11</sup>, Raimbault Patrick <sup>1</sup>, Ravel Christophe <sup>6</sup>, Rossi Vincent <sup>1</sup>, Rwawi Chaimaa <sup>1</sup>, Hlaili Asma Sakka <sup>13,14</sup>, Tesán-Onrubia Javier Angel <sup>15</sup>, Thomas Bastien <sup>2</sup>, Thyssen Melilotus <sup>1</sup>, Zaaboub Noureddine <sup>3</sup>, Garnier Cédric <sup>15</sup>

<sup>1</sup> Aix Marseille Univ., Université de Toulon, CNRS, IRD, MIO, Marseille, France

<sup>2</sup> Ifremer, CCEM Contamination Chimique des Ecosystèmes Marins, F-44311 Nantes, France

<sup>3</sup> Institut National des Sciences et Technologies de la Mer (INSTM), 28, rue 2 mars 1934, Salammbô 2025, Tunisia

<sup>4</sup> Université Paris Cité et Université Paris-Est Creteil, CNRS, LISA, F-75013 Paris, France

<sup>5</sup> IMT Nord Europe, Institut Mines-Télécom, Univ. Lille, Centre for Energy and Environment, F-59000 Lille, France

<sup>6</sup> Ifremer, Unité Littoral, Laboratoire Environnement Ressources Provence Azur Corse, Zone portuaire de Brégaillon, CS 20330, 83507 La Seyne-sur-Mer Cedex, France

<sup>7</sup> Environmental Sciences Program, Department of Biological and Environmental Sciences, College of Arts and Sciences, Qatar University, PO Box 2713, Doha, Qatar

<sup>8</sup> Aix Marseille Univ., CNRS, IRD, Collège de France, INRAE, CEREGE, 13545 Aix-en-Provence Cedex 4, France

<sup>9</sup> Laboratoire des Sciences du Climat et de l'Environnement LSCE/IPSL, CEA-CNRS-UVSQ, Université Paris-Saclay, 91191 Gif-sur-Yvette, France

<sup>10</sup> Department of Arctic and Marine Biology, UiT The Arctic University of Norway, Tromsø, Norway

<sup>11</sup> Institut de Radioprotection et de Sécurité Nucléaire (IRSN), PSE-SRTE-LRTA, Cadarache, France

<sup>12</sup> Université de Carthage, Faculté des Sciences de Bizerte, Bizerte, Tunisia

<sup>13</sup> Université de Tunis El Manar, Faculté des Sciences de Tunis, Laboratoire des Sciences de l'Environnement, Biologie et Physiologie des Organismes Aquatiques LR18ES41, Tunis, Tunisia

<sup>14</sup> Université de Carthage, Faculté des Sciences de Bizerte, Laboratoire de Biologie Végétale et Phytoplanctonologie, Bizerte, Tunisia

<sup>15</sup> Université de Toulon, Aix Marseille Univ., CNRS, IRD, MIO, Toulon, France

\* Corresponding author : Marc Tedetti, email address : [marc.tedetti@mio.osupytheas.fr](mailto:marc.tedetti@mio.osupytheas.fr)

---

**Abstract :**

This paper looks at experiential feedback and the technical and scientific challenges tied to the MERITE-HIPPOCAMPE cruise that took place in the Mediterranean Sea in spring 2019. This cruise proposes an innovative approach to investigate the accumulation and transfer of inorganic and organic contaminants within the planktonic food webs. We present detailed information on how the cruise worked, including 1) the cruise track and sampling stations, 2) the overall strategy, based mainly on the collection of plankton, suspended particles and water at the deep chlorophyll maximum, and the separation of these particles and planktonic organisms into various size fractions, as well as the collection of atmospheric deposition, 3) the operations performed and material used at each station, and 4) the sequence of operations and main parameters analysed. The paper also provides the main environmental conditions that were prevailing during the campaign. Lastly, we present the types of articles produced based on work completed by the cruise that are part of this special issue.

**Keywords :** Contaminants, Plankton, Mediterranean Sea, Size fractions, Bioaccumulation, Atmospheric deposition

76 **1. Introduction**

77

78 Plankton is recognised as a key gateway of inorganic and organic contaminants into the  
79 marine food web (Berroralbiz et al., 2011; Tao et al., 2018; Chauvelon et al., 2019; Li et al.,  
80 2021). Phytoplankton exposure to contaminants is mainly *via* water. Phytoplankton cells have  
81 a high surface area-to-volume ratio and thus large areas for exchanges, and consequently  
82 display high capacities for adsorbing and absorbing and thus bioconcentrating dissolved  
83 contaminants (Martin and Knauer, 1973; Fan and Reinfelder, 2003; Heimbürger et al., 2010;  
84 Lee and Fisher, 2016; Chauvelon et al., 2019). Contaminant bioconcentration in  
85 phytoplankton, thought to be governed mainly by partition equilibrium processes between the  
86 cells and the surrounding water (Frouin et al., 2013) even though cell growth conditions may  
87 prevent contaminants from reaching thermodynamic equilibrium (Swackhamer and Skoglund,  
88 1993), tends to increase with decreasing size of algal cells (Fan and Reinfelder, 2003).

89 Bioaccumulation processes in zooplankton are highly complex due to 1) entry of  
90 contaminants by both the water aqueous phase (bioconcentration) and diet, 2) trophic  
91 interactions and/or transfers between phytoplankton and herbivorous, carnivorous and  
92 omnivorous zooplankton, and 3) the contaminant elimination processes used by these  
93 organisms, including metabolization, excretion and passive release (Tiano et al., 2014;  
94 Alekseenko et al., 2018; Tao et al., 2018; Thomas et al., 2018; Li et al., 2020). The fact that  
95 all these processes can act simultaneously in the same or opposite directions makes it difficult  
96 to understand the variability of contaminant concentrations within the planktonic food web,  
97 which may ultimately display biomagnification (increasing contaminant concentrations with  
98 trophic level), bioreduction (decreasing contaminant concentrations with trophic level) or no  
99 clear pattern (Nizzetto et al., 2012; Tiano et al., 2014; Strady et al., 2015; Tao et al., 2017a, b;

100 [Alekseenko et al., 2018](#); [Chouvelon et al., 2019](#); [Tang et al., 2020](#); [Castro-Jiménez et al.,](#)  
101 [2021](#); [Li et al., 2021](#)).

102 One important biogeochemical implication of contaminant uptake by plankton is the  
103 role as a “biological pump” for contaminant sequestration ([Dachs et al., 2002](#); [Galbán-](#)  
104 [Malagón et al., 2012](#); [Duran and Cravo-Laureau, 2016](#); [González-Gaya et al., 2019](#); [Tang et](#)  
105 [al., 2020](#)). Contaminants bioconcentrated/bioaccumulated within planktonic organisms  
106 subsequently get transferred to higher trophic levels or to deep waters and sediment through  
107 sinking particles. During phytoplankton blooms, contaminant uptake by plankton depletes the  
108 contaminant loads in the dissolved phase of the water column and increases contaminant air-  
109 water fluxes, sinking particle fluxes and sequestration in sediments ([Berrojalbiz et al., 2011](#);  
110 [Nizzetto et al., 2012](#); [Everaert et al., 2015](#); [Morales et al., 2015](#); [Casal et al., 2017](#); [Ding et al.,](#)  
111 [2021](#)).

112 The phosphorus-limited Mediterranean Sea is globally classified as an oligotrophic  
113 marine area ([D’Ortenzio and d’Alcalà, 2009](#); [The Mermex Group, 2011](#); [Marañón et al.,](#)  
114 [2021](#)) dominated by small phytoplankton (i.e., pico- and nano-sized fractions) ([Uitz et al.,](#)  
115 [2006](#); [Hunt et al., 2017](#); [Mayot et al., 2017](#); [Leblanc et al., 2018](#); [Salhi et al., 2018](#); [Ramirez-](#)  
116 [Romero et al., 2020](#)), even though the occurrence of regional phytoplankton blooms (bloom  
117 bioregions, ecoregions; [D’Ortenzio and Ribera d’Alcalà, 2009](#); [Berline et al., 2014](#);  
118 [Reygondeau et al., 2017](#); [Ayata et al., 2018](#)) leads to periods of coexistence of numerous  
119 microalgal groups ([Siokou-Frangou et al., 2010](#); [El Hourany et al., 2019](#)).

120 Another feature of the Mediterranean Sea is its high exposure to chemical  
121 contamination ([Hinrichsen, 1990](#); [The Mermex Group, 2011](#); [UNEP, 2012](#)). Indeed, the  
122 intense human activities in its 23 bordering countries induce significant inputs of various  
123 chemical contaminants, while its semi-closed geography limits possibilities for diluting them.  
124 Contaminants are brought to the Mediterranean mainly by major and smaller river systems

125 (Elbaz-Poulichet et al., 2001; Radakovitch et al., 2008; Sicre et al., 2008; Guigue et al., 2014;  
126 Köck-Schulmeyer et al., 2021) but also *via* effluents, runoffs, groundwater, and maritime  
127 activities (Tedetti et al., 2010; Oursel et al., 2013; Tornero and Hanke, 2016; Fourati et al.,  
128 2018; Jacquet et al., 2021; Llamas-Dios et al., 2021) as well as atmospheric deposition  
129 (Lipiatou and Albaigés, 1994; Heimbürger et al., 2011; Castro-Jiménez et al., 2017; Barhoumi  
130 et al., 2018; Desboeufs et al., 2022). Studies have demonstrated that atmospheric deposition is  
131 the major source of contaminants in remote/open sea areas (Dachs and Méjanelle, 2010;  
132 González-Gaya et al., 2019; Jiskra et al., 2021; Cossa et al., 2022).

133         An interesting feature of the bioaccumulation of contaminants in the Mediterranean Sea  
134 is that the recorded contamination levels are significantly higher in its predatory species  
135 (crustaceans, sharks, teleost fish) than in congeneric species of the Atlantic Ocean (Cossa and  
136 Coquery, 2005; Bodiguel et al., 2009; Chauvelon et al., 2018). This difference may be related  
137 (but not solely) to the enhanced ability of the Mediterranean planktonic food webs to  
138 bioaccumulate certain contaminants, such as mercury (Hg) (Cossa and Coquery, 2005;  
139 Harmelin-Vivien et al., 2009; Chauvelon et al., 2018, 2019; Cossa et al., 2022), which further  
140 underscores the potential key role of the planktonic compartment in the transfer and  
141 accumulation of contaminants in the Mediterranean Sea. Furthermore, contaminant-plankton  
142 interactions in the Mediterranean Sea are expected to evolve in the coming years, as it has  
143 been identified as a hotspot for climate change due to its high reactivity to external forcing,  
144 particularly variations in water, energy and matter fluxes that will affect its circulation,  
145 biogeochemical fluxes and ecosystem functioning (Lejeusne et al., 2010; The Mermex Group,  
146 2011; Ser-Giacomi et al., 2020).

147         However, there are still key gaps in our understanding around the actual ability of  
148 plankton to accumulate and transfer contaminants (i.e., the role of plankton as a biological  
149 pump of contaminants), especially its small size fractions, i.e., pico- and nano-plankton. This

150 lack of knowledge partly comes from methodological difficulties in: 1) collecting and  
151 separating plankton into its various size fractions from pico- to macro-plankton, separating  
152 bacterio-, phyto- from zoo-plankton, and separating non-living suspended particulate matter  
153 from plankton, 2) obtaining sufficient material in each of these fractions to perform trace-  
154 level chemical analyses, and 3) clearly identifying the trophic relationships between  
155 planktonic size fractions in the presence of detritus (particularly in smaller size fractions) and  
156 mixing of different trophic levels within each size fraction.

157 In this context, the MERITE-HIPPOCAMPE cruise aimed to evaluate the accumulation  
158 and transfer of a hugely diverse range of inorganic and organic contaminants at the  
159 atmosphere-water-plankton interfaces and within the planktonic food webs, i.e., phyto-, zoo-  
160 and bacterio-plankton, along a North-South transect in the Mediterranean Sea. This ultimately  
161 to quantify the role of Mediterranean plankton as a biological pump of contaminants, focusing  
162 on contaminant transfers into the planktonic food webs. The main collection area for  
163 plankton, suspended particles and water is the deep chlorophyll maximum (DCM), which may  
164 be considered as the layer with the highest biomasses of plankton, mainly phytoplankton, but  
165 also zooplankton. The plankton size fractions investigated include pico- (0.2–2  $\mu\text{m}$ ), nano-  
166 (2–20  $\mu\text{m}$ ), micro- (20–200  $\mu\text{m}$ ) and meso-plankton (200–2000  $\mu\text{m}$ ). The contaminants  
167 examined are trace metals, organometals and metalloids (As, Cd, Cr, Cu, Fe, Hg, MeHg, Mn,  
168 Ni, Pb, Sb, Zn...), organic contaminants (PAHs, PCBs, PBDEs, PFASs), radionuclides  
169 ( $^{137}\text{Cs}$ ), and microplastics. The specific objectives of the cruise are: 1) to determine the  
170 contaminant concentration levels in various planktonic compartments (phyto-, zoo- and  
171 bacterio-plankton), suspended particles and water (dissolved phase), as well as atmosphere  
172 and, 2) to assess the role of dry/wet atmospheric deposition as a source of contaminants for  
173 marine waters, especially in offshore areas, 3) to gauge how contaminant accumulations and  
174 transfers are influenced by plankton in terms of size and community structures, trophic

175 interactions and biochemical content, and 4) to establish the link between habitat  
176 characteristics and concentration levels of contaminants in plankton. The questions addressed  
177 by the MERITE-HIPPOCAMPE cruise are summarised in [Fig. 1](#). In this paper, we first  
178 present the implementation of the cruise project in terms of strategy, study stations, material  
179 used, operations performed, sequence of operations, and main parameters analysed. We then  
180 work up from a joint dataset to provide the main meteorological, hydrological, and  
181 biogeochemical conditions prevailing during the cruise. Lastly, we introduce the types of  
182 articles produced through the MERITE-HIPPOCAMPE cruise that are part of this special  
183 issue.

184

185

## 186 **2. Implementation of the cruise**

187

### 188 **2.1. Research strategy**

189 The overall research strategy for our oceanographic cruise was as follows:

190 1) Investigate areas of contrasted ecological characteristics in the north and south of the  
191 Mediterranean Sea. The selected period was the spring bloom, crossing primary production  
192 and bloom areas as defined by [D’Ortenzio and d’Alcalà \(2009\)](#) as well as various fishing  
193 zones, urbanised bays, and consensus regions as defined by [Ayata et al. \(2018\)](#) ([Fig. 2a, b](#);  
194 [Fig. S1](#)).

195 2) Characterise the water column in these sampling sites in terms of physical and  
196 biogeochemical properties through *in situ* physical and optical measurements, and determine  
197 the DCM.

198 3) Implement ultra-clean on-board conditions for the collection and treatment of water  
199 and plankton samples for ultra-trace-level analyses of inorganic and organic contaminants.

200 4) Collect large amounts of plankton, suspended particles, and water (dissolved phase)  
201 in the DCM and, in a lesser extent, surface/subsurface waters (0–5 m depth) (Fig. 3). The  
202 choice of focusing our sampling on the DCM was motivated by the need to 1) collect a high  
203 biomass of plankton from the same location to determine the concentration levels of a wide  
204 range of contaminants, and over a broad spectrum of planktonic size fractions, and 2) be  
205 located in a relevant area for pelagic trophic interactions in both the coastal and marine areas.

206 5) Separate these large amounts of plankton and particles into various size fractions  
207 (from 0.2  $\mu\text{m}$  to  $> 2000 \mu\text{m}$ ) by filtration or sieving (Fig. 3).

208 6) Share the size fractioned samples for analysis of a battery of parameters, including (i)  
209 contaminants, with trace metals, organometals and metalloids (As, Cd, Cr, Cu, Fe, Hg, MeHg,  
210 Mn, Ni, Pb, Sb, Zn, etc.), organic contaminants (PAHs, PCBs, PBDEs, PFASs), radionuclides  
211 ( $^{137}\text{Cs}$ ) and microplastics, (ii) biomass, size structure, taxonomy, cytometry, diversity and  
212 pigment composition of plankton, and (iii) biogeochemical parameters, with nutrients, total  
213 chlorophyll *a* (TChl*a*), suspended particulate matter (SPM), dissolved and particulate organic  
214 matter, C and N isotopic ratios ( $\delta^{13}\text{C}$ ,  $\delta^{15}\text{N}$ ), and biochemical compounds (carbohydrates,  
215 proteins, lipids) (Fig. 3).

216 7) Combine several methods (taxonomy, optical measurements, chemical analyses) to  
217 tentatively distinguish the contributions of living (plankton) and non-living (detrital) materials  
218 to contaminant accumulation and transfers.

219 8) Collect on-board samples of atmospheric wet deposition (rain) to assess their  
220 potential importance as a source of contaminants for marine water and plankton. The  
221 collection of atmospheric samples was also done in parallel on the coast by setting up two  
222 ground stations, located in the northern part (Marseille, France) and southern part (Sfax,  
223 Tunisia) of the Mediterranean basin (Fig. 2a), in which atmospheric total (dry and wet)



224 deposition were measured on a regular (bi-monthly or monthly) basis from March 2019 to  
225 June 2020, i.e., before, during, and after the oceanographic cruise.

226 9) Sample small pelagic plankton-feeding fishes in Tunisian waters (see sampling  
227 positions in Fig. 2a). The fish samples were analysed for a number of contaminants in order to  
228 set bioaccumulation factors for higher trophic levels.

229

## 230 **2.2. Cruise track and study stations**

231 The MERITE-HIPPOCAMPE cruise took place in spring 2019, from April 13 to May  
232 14, on board the French Research Vessel (R/V) *Antea* along a North-South transect (round  
233 trip) in the Mediterranean Sea, from the French coast (La Seyne-sur-Mer, Northwestern  
234 Mediterranean) to the Gulf of Gabès in Tunisia (Southeastern Mediterranean) (Tedetti and  
235 Tronczynski, 2019) (Fig. 2a, b). Leg 1 (13–28 April 2019) ran the southward transect,  
236 between La Seyne-sur-Mer and Tunis, with sampling at five stations: St2, St4, St3, S10, and  
237 St11 (in this chronological order). Leg 2 (30 April–14 May 2019) covered first the end of the  
238 southward transect (from Tunis to the Gulf of Gabès), and then the return trip back northward  
239 from the Gulf of Gabès to La Seyne-sur-Mer. Five stations were sampled during leg 2: St15,  
240 St17, St19, St9 and St1 (in this chronological order). Five stations (St1–St4, St9) were  
241 situated in the French area, two stations (St10, St11) in the Italian area, and three stations  
242 (St15, St17, St19) in the Tunisian area (Fig. 2a, b; Table 1).

243 The ten stations were chosen according to different criteria based on physical,  
244 biogeochemical and biological conditions and anthropogenic pressures (Fig. 2a; Fig. S1;  
245 Table 1). St1 and St4 were located in the urbanised bays opposite the cities of Toulon and  
246 Marseille, respectively, and thus submitted to strong anthropogenic pressures. St4 was the  
247 SOLEMIO station, which is part of the French national coastal observation monitoring  
248 network SOMLIT (<http://somalit.epoc.u-bordeaux1.fr/fr/>). St1 and St4 were “intermittent

249 bloom” areas or “bloom” areas according to [D’Ortenzio and d’Alcalà \(2009\)](#) based on  
250 SeaWiFS satellite observations of surface TChl $a$  concentration. St2 and St3 were situated  
251 offshore of Toulon and Marseille, respectively. St2 was at the limit of the continental shelf  
252 and the boundary of the Ligurian consensus region ([Ayata et al., 2018](#)) ([Fig. S1](#)). St3, situated  
253 at the southeast entrance to the Gulf of Lion’s continental shelf, was the JULIO station, which  
254 is dedicated to the study of intrusions of the Ligurian-Provençal current ([Barrier et al., 2016](#)).  
255 St2 and St3 were considered “intermittently bloom” areas or “bloom” areas ([D’Ortenzio and](#)  
256 [d’Alcalà, 2009](#)). These stations (St1–St4) have hosted in the past or continue to host visits  
257 serving several monitoring networks such as SOMLIT and ROMARIN, and projects  
258 including MERMEX-MERITE, COSTAS and IBISCUS.

259 St9 corresponds to offshore station 1 of the PEACETIME cruise ([Guieu et al., 2020](#)). It  
260 was located north of the North Balearic thermal Front (NBF), at the boundary of the Ligurian  
261 consensus region ([Ayata et al., 2018](#)), in the winter convection area ([Fig. S1](#)). The NBF,  
262 which is one of the main consensus frontiers of the Mediterranean Sea ([Ayata et al., 2018](#)), is  
263 found between the Balearic Islands and Sardinia, but its position spans a large area and can  
264 vary with wind conditions and seasons ([Barral et al., 2021](#)). St10 (offshore station 2 of the  
265 PEACETIME cruise) was situated south of St9, very close to the NBF. Although St10 was  
266 positioned south of the average position of the NBF, it was in fact located slightly north of the  
267 front which had moved further south during the sampling period ([Rwawi et al., in prep.](#)). St11  
268 (offshore station 3 of the PEACETIME cruise) was plainly positioned south of the NBF, in  
269 the Algerian consensus region ([Ayata et al., 2018](#)) ([Fig. S1](#)). St10 and St11 were characterised  
270 by the presence of intense mesoscale eddies: St10 was rather situated between one  
271 anticyclonic and one cyclonic eddy, while St11 was located within an anticyclonic eddy  
272 ([Rwawi et al., in prep.](#)). St9, St10, and St11 are referred to as “bloom”, “intermittent bloom”

273 and “no bloom” areas, respectively, according to the [D’Ortenzio and d’Alcalà \(2009\)](#) system  
274 ([Fig. 2a](#); [Table 1](#)).

275 St15, situated in the Gulf of Hammamet (Tunisia), was close to the Sicily Channel,  
276 which plays host to the exchanges between the two (Western and Eastern) Mediterranean  
277 basins, and submitted to the possible entrance of the Atlantic Tunisian Current branch, also  
278 called the Atlantic-Ionian stream. St17 (north of the Gulf of Gabès) and St19 (south of the  
279 Gulf of Gabès) were located at the boundary of and within the Gabès consensus region,  
280 respectively ([Ayata et al., 2018](#)) ([Fig. S1](#)), and are typified by shallow waters, strong  
281 influences of tidal pull (the highest of the Mediterranean; amplitude > 2 m) and the Atlantic  
282 Tunisian Current. St17 and St19 are also characterised by nutrient inputs from Saharan dust  
283 deposition or sediment resuspension and the resulting high planktonic productivity levels  
284 ([Béjaoui et al., 2019](#)). Moreover, given its cumulative index of warming, overfishing and  
285 pollution effects, the Gulf of Gabès has recently been recognised as a hotspot of  
286 anthropogenic pressures within the Mediterranean Sea ([Reygondeau et al., 2014](#)). St15, St17  
287 and St19 were zones marked by a high density of small pelagic fish and considered as “no  
288 bloom” (St15) or “coastal bloom” areas (St17, St19) based on the [D’Ortenzio and d’Alcalà](#)  
289 [\(2009\)](#) system. These stations (St15-St19) have been investigated in the past in the framework  
290 of the Tunisian POEMM and ESSATEL programs ([Fig. 2a](#); [Fig. S1](#); [Table 1](#)).

291 Due to rough sea conditions that occurred during sampling of St19 (south of the Gulf of  
292 Gabès; [Fig. 2a, b](#)), the ship went to shelter, first off the island of Djerba and then off the city  
293 of Zarzis ([Fig. 2a, b](#)), before returning to station St19 to finish work between May 3 and 4.  
294 During the transit between off Djerba and off Zarzis, atmospheric deposition sampling was  
295 carried out following an intense episode of Saharan dust deposition.

296 Besides the ten stations prospected from the R/V *Antea*, two other stations (T2 and T4)  
297 were sampled in the Tunisian waters during leg 2 (2–3 May 2019) on board the R/V *Hannibal*

298 for trawling small pelagic fishes. T2 was located in the Gulf of Gabès not far from St19,  
299 whereas T4 was situated in the Gulf of Tunis. The duration of trawling was 40 min at T2 and  
300 90 min at T4 (Fig. 2a; Table 2). The fish species captured by trawling were anchovy, sardine,  
301 sardinella, and mackerel (Lajnef et al., in prep.).

302

### 303 **2.3. Equipment and operations**

304 At each of the ten stations, the following sampling equipment was deployed and the  
305 following operations were performed at sea and on board the R/V *Antea*.

#### 306 *2.3.1. Water sampling with Niskin and Go-Flo bottles and subsequent in-line*

307 *filtration*. A trace metal-clean carousel equipped with ten 12-L bottles (1 Niskin, 5 Niskin X,  
308 4 Go-Flo) and a conductivity-temperature-depth probe (CTD; Seabird SBE 911*plus*),  
309 mounted with photosynthetically available radiation (PAR) (Biospherical), TChla  
310 fluorescence (Aqua Tracka, Chelsea ctg), dissolved oxygen (O<sub>2</sub>) (SBE 43), dissolved organic  
311 matter (DOM) fluorescence (WETStar, WETLabs) and transmittance (C-Star, WETLabs)  
312 sensors, was deployed from the ship's moon pool *via* the electro-mechanical (conducting)  
313 cable (Table S1; Fig. S2a). Vertical profiles were collected over the depth range 0–250 m or  
314 surface-to-bottom when depth was < 250 m, and seawater was sampled at two depths: 5 m or  
315 the DCM identified based on TChla profiles. Seven bottles (4 Niskin X and 3 Go-Flo) were  
316 dedicated to DCM sampling, while three bottles (1 Niskin, 1 Niskin X and 1 Go-Flo) were  
317 used for 5-m-depth sampling. The Go-Flo bottles were lowered into the water in open  
318 position. At St9 and St10, sampling was also conducted down to 500-m depth to collect  
319 seawater in the oxygen minimum zone (OMZ) identified based on O<sub>2</sub> profiles. At St9, water  
320 was collected at 5 m, DCM and 440 m (identified as OMZ), whereas at St10 sampling was  
321 carried out at 5 m, DCM, 100, 200, 300, 400 m (identified as OMZ) and 500 m. The Niskin X  
322 bottles used here (model 101012X) are Niskin with a completely free Teflon-coated sample

323 chamber, Teflon-coated and externally-located stainless steel end plug closure springs, as well  
324 as Teflon-coated air valves and drainage taps. Before the cruise, all ten bottles were  
325 thoroughly washed with hydrochloric acid (HCl) 1 M, demineralized water and ultra-pure  
326 water (i.e., Milli-Q water from Millipore system, final resistivity of 18.2 MΩ cm). Before  
327 sampling, they were rinsed with seawater collected at 50-m and 170-m depth at the first  
328 station (St2). Between two casts, working on the deck of the ship, we covered the drainage  
329 taps and the top (upper stoppers) of the bottles with plastic bags to avoid any sample  
330 contaminations.

331         Once on board, after water collection at 5-m depth and in the DCM, the carousel with  
332 all the bottles was placed in the wet laboratory for in-line filtration (Table S1; Fig. S2b). For  
333 that purpose, the bottles were pressurised to 0.5 bar with argon (UN1006, compressed, 2.2)  
334 piped in using a silicon tubing system and quick-connect gas fittings replacing bottle air  
335 valves. The upper and lower stoppers of the Niskin bottles were held tight by home-made  
336 pairs of high-density polyethylene (HDPE) rods and clamps screwed at the top and bottom. A  
337 10-cm-long piece of acid-cleaned silicon tubing was inserted into the drainage tap of each  
338 bottle, and a perfluoroalkoxy (PFA) filter holder (Savillex®, 25 or 47-mm diameter) was  
339 connected to the tubing. A graduated container collecting the filtered water served to indicate  
340 the exact volume filtered on each filter.

341         In-line filtration makes it possible to effectively filter large quantities of water in clean  
342 conditions and to recover the filters and filtered water samples for a battery of analyses.  
343 Filtration was done on pre-combusted (450 °C, 6 h), pre-weighed glass fibre filters (GF/F,  
344 Whatman) of 25 or 47-mm diameter (pore size: ~ 0.7 μm) for analyses of TChla, pigments,  
345 SPM, particulate organic carbon (POC), particulate organic nitrogen (PON), stable isotopes of  
346 carbon and nitrogen ( $\delta^{13}\text{C}$ ,  $\delta^{15}\text{N}$ ), biochemical compounds (carbohydrates, lipids, proteins)  
347 and Hg on the size fraction > 0.7 μm. SPM measurements were done on (pre-weighed) 25-

348 mm and 47-mm-diameter GF/F filters rinsed with ultra-pure water after filtration in order to  
349 remove salts, but also on (pre-weighed) 47-mm-diameter GF/F filters that had not been rinsed  
350 with ultra-pure water (for which the amount of salts was estimated). Filtration was also done  
351 on pre-cleaned 0.2- $\mu\text{m}$ -pore-size 47-mm-diameter mixed cellulose esters (MCE) filters for the  
352 analyses of trace metals/metalloids and microbial diversity on the size fraction  $> 0.2 \mu\text{m}$ , and  
353 on 0.8- $\mu\text{m}$ -pore-size 47-mm-diameter pre-cleaned MCE filters for the analyses of copper (Cu)  
354 and zinc (Zn) isotopes on the size fraction  $> 0.8 \mu\text{m}$ . GF/F-filtered seawater ( $< 0.7 \mu\text{m}$ ) was  
355 used for the analyses of nutrients, i.e., silicates [ $\text{Si}(\text{OH})_4$ ], nitrates ( $\text{NO}_3^-$ ), nitrites ( $\text{NO}_2^-$ ),  
356 phosphates ( $\text{PO}_4^{3-}$ ) and ammonium ( $\text{NH}_4^+$ ), dissolved organic carbon (DOC), and absorption  
357 of chromophoric DOM ( $a_{\text{CDOM}}$ ), whereas 0.2- $\mu\text{m}$ -filtered seawater was used for the analyses  
358 of dissolved trace metals/metalloids and Hg (Fig. 3; Table S1). Volume of seawater filtered  
359 ranged from 600 mL (25-mm GF/F filter for TChl*a*) to 12 L (47-mm GF/F filter for POC,  
360 PON,  $\delta^{13}\text{C}$ ,  $\delta^{15}\text{N}$ , and biochemical compounds).

361 Raw (unfiltered) seawater was taken for the analyses of total trace metals/metalloids  
362 and Hg/MeHg, while seawater pre-filtered onto 100- $\mu\text{m}$  silk was collected for phytoplankton  
363 taxonomy and cytometry analyses. Raw seawater from the DCM was also used to perform on-  
364 board experiments on microbial methylation/demethylation of Hg (at selected stations), while  
365 raw seawater collected at 5-m depth and in the DCM at St1, St9, S15 and St19 was used to  
366 conduct dilution experiments (see section 2.3.8). Most of these filtrations were also conducted  
367 on OMZ water (at St9 and St10) for the same analyses. Raw and 0.2- $\mu\text{m}$ -filtered seawater at  
368 the different depths was also used for shipboard analyses of Hg (see section 2.3.9) (Table S1).  
369 Filter blanks were regularly run during the cruise: filters were treated as sample filters, either  
370 without passing any water on them or by rinsing with ultra-pure water, depending on the  
371 parameter. Detailed information on the in-line filtration from Go-Flo and Niskin bottles,  
372 including storage of samples, can be found in Fig. S3.

373           2.3.2. *In situ optical measurements.* A small CTD unit (SBE 19*plus*) equipped with  
374 a TChl*a* fluorescence sensor (WETStar, WETLabs) was deployed from the moon pool on the  
375 hydrographic cable, over the same depth range as the carousel (0–250 m or 0–bottom), to  
376 timely determine the depth of the DCM between different sampling operations, in particular  
377 just before McLane *in situ* pumps (see [section 2.3.3](#)) and MultiNet deployments (see [section](#)  
378 [2.3.5](#)) ([Table S1](#)).

379           A laser optical plankton counter (LOPC, Rolls Royce) and laser *in situ* scattering  
380 transmissometry-Holography (LISST-HOLO, Sequoia Scientific) were used together, fixed  
381 on a small carousel, to provide information on the abundances and size spectra of particles  
382 and plankton (> 20  $\mu\text{m}$  for LISST-HOLO, > 100  $\mu\text{m}$  for LOPC). Both systems were deployed  
383 from the moon pool on the hydrographic cable. Vertical profiles were performed over the  
384 depth range 0–250 m or 0–bottom ([Table S1](#); [Fig. S2c](#)).

385           2.3.3. *In situ filtration with McLane pumps.* Four McLane Large Volume Water  
386 Transfer System Samplers (WTS6-142LV, 4–8 L min<sup>-1</sup>), hereinafter referred to as McLane *in*  
387 *situ* pumps, were used to collect large amounts of particles and plankton over different size  
388 fractions in the DCM. The four pumps were attached together with clamps and chains, and  
389 deployed at the same time from the moon pool on the hydrographic cable to reach the DCM  
390 ([Fig. S2d](#)). Pumping lasted between 40 and 60 min, giving an average ~ 240 L of water  
391 filtered by each pump. Three successive casts of the four-pump system were carried out,  
392 giving a total of 12 pumping runs done at each station ([Table S1](#)).

393           Three pumps (A, B, C) were each mounted with a regular 142-mm filter-holder  
394 (“McLane holder”) holding one 142-mm-diameter filter: one ~ 0.7- $\mu\text{m}$ -pore-size pre-  
395 combusted pre-weighed GF/F filter, one 0.8- $\mu\text{m}$ -pore-size pre-cleaned MCE filter, or one 20-  
396  $\mu\text{m}$ -pore-size pre-cleaned Nylon filter. After installing the filters, the three McLane holders  
397 were covered with a 60- $\mu\text{m}$ -pore-size sock-type pre-filter so that the filtered particles size

398 fractions were 0.7–60, 0.8–60 and 20–60  $\mu\text{m}$ . At three casts each, pumps A, B and C were  
399 able to sample nine filters for analysis of TChl*a*, SPM, POC, PON,  $\delta^{13}\text{C}$ ,  $\delta^{15}\text{N}$ , biochemical  
400 compounds, PAHs, PCBs, PBDEs and Hg/MeHg on the GF/F filters (0.7–60- $\mu\text{m}$  size  
401 fraction), analysis of trace metals/metalloids, Cu and Zn isotopes and microbial diversity on  
402 the MCE filters (0.8–60- $\mu\text{m}$  size fraction), and analysis of microplastics on the Nylon filters  
403 (20–60- $\mu\text{m}$  size fraction) (Fig. 3; Table S1; Fig. S4).

404 The fourth pump (D) was mounted with a mini-Multiple Unit Large Volume in-situ  
405 Filtration System (MULVFS) filter holder composed of baffle tubes on the top followed by  
406 successive baffle and filter support plates, for sequential filtration with three different filters  
407 (142-mm diameter) (Bishop and Wood 2008; Bishop et al., 2012). The baffles were designed  
408 to straighten the flow, suppress turbulence, and distribute particles evenly across the filter.  
409 The filter series used were either 1) one  $\sim$  0.7- $\mu\text{m}$ -pore-size pre-combusted, pre-weighed  
410 GF/F filter, one 2.7- $\mu\text{m}$ -pore-size pre-combusted, pre-weighed GF/D filter, and one 20- $\mu\text{m}$ -  
411 pore-size pre-cleaned Nylon filter, or 2) one 0.8- $\mu\text{m}$ -pore-size pre-cleaned MCE filter, one 3-  
412  $\mu\text{m}$ -pore-size pre-cleaned MCE filter, and one 20- $\mu\text{m}$ -pore-size pre-cleaned Nylon filter.  
413 With its three casts, pump D was able to collect nine filters for the analysis of TChl*a*, SPM,  
414 POC, PON,  $\delta^{13}\text{C}$ ,  $\delta^{15}\text{N}$ , biochemical compounds, and Hg/MeHg on the 0.7–2.7, 2.7–20, and >  
415 20- $\mu\text{m}$  size fractions, and trace metals/metalloids on the 0.8–3, 3–20, and > 20- $\mu\text{m}$  size  
416 fractions (Fig. 3; Table S1; Fig. S4).

417 SPM measurements were made on (pre-weighed) 142-mm GF/F, GF/D and Nylon  
418 filters rinsed with ultra-pure water after filtration in order to remove residues of the seawater  
419 salts, but also on (pre-weighed) 142-mm GF/F filters not rinsed with ultra-pure water (for  
420 which the amount of salts was estimated). All filters were placed in glass boxes, plastic boxes  
421 or aluminium foil, depending on the parameter, and stored on board at  $-20\text{ }^{\circ}\text{C}$  (Fig. S2e, f;  
422 Fig. S4). A special support was purpose-designed to accommodate/fix the filter holders in the



423 wet laboratory to facilitate the process of preparing the filters before deployment, and then  
424 handling, rinsing with ultra-pure water or direct drying (by connecting the filter holder to a  
425 vacuum pump) the filters after deployment (Fig. S2e, f). Before pump deployment, all the  
426 filter holder and filter systems were rinsed with ultra-pure water. Filter blanks were done at  
427 regular intervals during the cruise.

#### 428 *2.3.4. Water sampling and subsequent in-line filtration with an ASTI pump.*

429 Seawater was also sampled at ~ 10–20-m depth with a pneumatically-operated Teflon ASTI  
430 pump (model PFD2) set up on board and connected to Teflon tubing, which was weighted  
431 down and immersed from port side with the hydrology gallows (Table S1). The pumped  
432 seawater was filtered in-line onto a pre-combusted 142-mm GF/F filter using a 142-mm  
433 Teflon filtration holder. This filtration took place in the clean lab container (IFREMER,  
434 CNXU 300022/1) installed on the rear deck of the ship. Part of the filtered seawater was  
435 stored in three 20-L stainless steel jerrycans, while the other part was stored in a metal-free  
436 50-L plastic container. This filtered seawater was used for sieving the large quantities of  
437 plankton collected with the Multiple Plankton Sampler. The filtered seawater stored in two of  
438 the stainless steel jerrycans was used exclusively for sieving on a stainless steel sieve column  
439 to obtain plankton samples for organic parameter analyses, and the filtered seawater stored in  
440 the plastic container was used exclusively for sieving on a nylon sieve column for analyses of  
441 inorganic parameters (see section 2.3.5). Filtered seawater from the third jerrycan was  
442 amended with 50 mL of dichloromethane, then shaken and degassed and stored in the  
443 container at ambient temperature for subsequent analyses of dissolved (< 0.7 µm)  
444 hydrocarbons (Guigue et al., in prep.) (Fig. 3; Table S1). All seawater containers (stainless  
445 steel and plastic) were rinsed several times with filtered seawater before sample collection.

#### 446 *2.3.5. Plankton sampling with a MultiNet and subsequent sieving.*

447 A Multiple Plankton Sampler (Midi type, Hydro-Bios), referred to hereafter as “MultiNet”, was

448 employed to collect plankton in the DCM. The MultiNet was composed of 5 individual  
449 (exchangeable) 2.5-m-long nets with 0.25-m<sup>2</sup> apertures, a 60- $\mu$ m mesh size, and cod ends of  
450 the same mesh size, together with two Hydro-Bios flowmeters (one into the mouth and the  
451 other on the side) to assess the volume of water filtered by the nets, plus a CTD sensor and a  
452 TChl $a$  fluorometer (Chelsea ctg). The MultiNet was connected *via* the electro-mechanical  
453 cable to the operating computer to enable online monitoring of sensor feedback and opening  
454 and closing of the nets, mainly based on flowmeter data and the amount of water passing  
455 through the open net. It was operated from the stern A-frame. Since the device was deployed  
456 horizontally in the DCM, the usual configuration (for vertical casts) was modified with a V-  
457 fin deflector attached below the MultiNet and the five cod ends attached using a helicoidal  
458 bucket connector (Fig. S2g, h). Ship speed while towing the MultiNet was ~ 2 knots (Table  
459 S1). Once the five nets were filled (after 30 to 100 min depending on the station), the  
460 MultiNet was hauled back on board, the cod ends were rinsed out with local seawater, and  
461 their content was transferred to pre-cleaned 10-L HDPE bottles. The instrument was then  
462 returned to the water. This operation (“cast”) had to be repeated several times (between two  
463 and eight horizontal casts, depending on the station) until we got sufficient amounts of  
464 plankton. At St19, due to technical issues, the MultiNet was replaced by a square net with a 1-  
465 m<sup>2</sup> aperture mounted with single 60- $\mu$ m mesh-size net. Total filtered water volume with the  
466 MultiNet/square net ranged from 314 (St2) to 2373 m<sup>3</sup> (St10).

467 In the clean on-board container lab, plankton collected in HDPE bottles was then size-  
468 fractionated on 1) a column of five stainless steel sieves (60, 200, 500, 1000 and 2000- $\mu$ m  
469 mesh-size) by wet-sieving with the GF/F filtered seawater stored in stainless steel jerrycans  
470 for subsequent analyses of organic parameters, and 2) a column of five nylon sieves (60, 200,  
471 500, 1000 and 2000- $\mu$ m mesh-size) by wet-sieving with the GF/F filtered seawater stored in  
472 the plastic container for the subsequent analyses of inorganic parameters (Fig. S2i, j). The

473 filtered seawater was routed with a gentle flow to the top of the sieve column by the ASTI  
474 pump using Teflon tubing. The plankton size fractions recovered on the stainless-steel sieves  
475 were shared out and transferred to pre-combusted glass flasks for the analyses of POC, PON,  
476  $\delta^{13}\text{C}/\delta^{15}\text{N}$ , biochemical compounds, PAHs, PCBs, PBDEs and PFASs, or to plastic flasks for  
477 zooplankton taxonomy and imagery, TChla (60–200- $\mu\text{m}$  size fraction only) and microbial  
478 diversity (60–200 and 200–500- $\mu\text{m}$  size fractions only). The plankton size fractions recovered  
479 on the nylon sieves were shared out and transferred to pre-cleaned polypropylene flasks for  
480 the analyses of trace metals/metalloids, Hg and  $^{137}\text{Cs}$  (Fig. 3; Table S1; Fig. S5). Planktonic  
481 biomass (in  $\text{mg m}^{-3}$  dry weight) was also determined in each of the size fractions (Fierro-  
482 González et al., 2023). All samples were stored at  $-20\text{ }^{\circ}\text{C}$  except those for zooplankton  
483 taxonomy that were stored at ambient temperature after adding buffered formalin (Fig. S5).

484 *2.3.6. Plankton and micro-plastic sampling with Triple and Manta nets.* A triple  
485 net, equipped with 60, 120 and 200- $\mu\text{m}$  mesh-sized nets each with 0.60-m aperture diameter  
486 was used to undertake two vertical tows over the depth 0–200 m (or 0–bottom if depth < 200  
487 m), i.e., one tow for biomass, and one tow for taxonomy and imagery. The device was  
488 deployed from port side using hydrology gallows (Table S1; Fig. S2k). After collection, the  
489 cod-end contents from each of the three nets (first tow) were passed through GF/F filters that  
490 were stored in Petri dishes at  $-20\text{ }^{\circ}\text{C}$  for biomass measurements, while the cod-end contents  
491 from the second tow were passed through a 60- $\mu\text{m}$  sieve for volume reduction and transferred  
492 to 250-mL plastic tubes amended with 12.5-mL buffered formalin for taxonomy and imagery  
493 analyses. At St1, St9, S15 and St19, the contents of the 200- $\mu\text{m}$  net were also collected to  
494 analyse chlorophyll gut-contents of mesozooplankton (see section 2.3.8).

495 Two Manta nets were used for horizontal tows in surface waters: one a 330- $\mu\text{m}$  mesh  
496 size (1 tow, 3 knots, 20 min max) for microplastic analyses, and the other a 60- $\mu\text{m}$  mesh size  
497 (1 tow, 1 knot, 10 min max) for microplastics and plankton (neuston) analyses, both deployed

498 from port side using hydrology gallows (Table S1). After collection, the content of the 330-  
499  $\mu\text{m}$  Manta net was sieved successively through 5000 and 300- $\mu\text{m}$  mesh-size sieves (if large  
500 items were present in the collectors) and transferred to a 1-L glass bottle added with formalin  
501 (4% final concentration). The content of the 60- $\mu\text{m}$  Manta net was transferred to a 1-L glass  
502 bottle added with 50-mL buffered formalin.

503 *2.3.7. In-line filtration onto cartridges.* At each station, in-line filtration was carried  
504 out in the wet laboratory on seawater collected continuously at 2-m depth by the shipboard  
505 pump system (Table S1). Two polypropylene cartridges (Polycap HD), the first with a 20- $\mu\text{m}$   
506 pore size and the second with a 0.45- $\mu\text{m}$  pore size, were mounted in series to recover the  
507 0.45–20- $\mu\text{m}$  and > 20- $\mu\text{m}$  size fractions. Around 1000 L of seawater was filtered on the two  
508 cartridges at each station. The dissolved fraction (< 0.45  $\mu\text{m}$ ) was collected in 20-L plastic  
509 containers. These samples served for radionuclide analyses ( $^{137}\text{Cs}$ ) (Radakovitch et al., in  
510 prep.).

511 *2.3.8. Dilution experiments.* At St1, St9, S15 and St19, seawater collected from the  
512 carousel bottles at 5-m depth and in the DCM was used to perform dilution experiments by  
513 means of a thermostatic incubation chamber (Table S1). These experiments were  
514 implemented to assess the phytoplankton production rates and microzooplankton grazing  
515 rates. At the same stations, the contents of the 200- $\mu\text{m}$  Triple nets (vertical tows) were used to  
516 analyse the chlorophyll gut contents of mesozooplankton by fluorescence in order to estimate  
517 the impact of mesozooplankton grazing on large phytoplankton (i.e., nano- and micro-  
518 phytoplankton). These experiments and measurements served to determine the carbon fluxes  
519 and type and structure of the planktonic food webs (Medebb et al., in prep.).

520 *2.3.9. Shipboard analyses.* Unfiltered and 0.2- $\mu\text{m}$ -filtered seawater collected from  
521 the carousel bottles at 5-m depth, in the DCM and at the other depths (profiles, OMZ) served  
522 for shipboard analyses of total and purgeable Hg using a Tekran® auto-analyser (model 2500),

523 consisting in purge and trap of volatilized Hg species followed by cold vapour atomic  
524 fluorescence spectrometry (CVAFS) detection (Table S1; Fig. S2m).

525 A part of the seawater collected continuously at 2-m depth by the shipboard pump  
526 system was subsampled and routed to a CytoSense® automated flow cytometer (CytoBuoy)  
527 installed in the dry laboratory. The CytoSense was employed to analyse (in terms of  
528 identification and abundance) individual or colonial phytoplankton cells sized between 0.8  
529 and 800 µm. Cytometry measurements were carried out continuously at the different stations  
530 but also all along the transect (Table S1; Fig. S2l; Boudriga et al., 2022).

531 *2.3.10. Atmospheric deposition.* During the cruise, wet atmospheric deposition  
532 samples were collected using two rain collectors placed in PVC pipes that were fixed at the  
533 front of the ship (10 m above sea level). The collector for trace metal samples was composed  
534 of an acid pre-cleaned, metal-free plastic bottle and funnel (Fig. S2n). The collector for PAH  
535 samples was composed of a pre-combusted amber glass bottle and glass funnel (Table S1;  
536 Fig. S2o). Overall, six rainwater samples were collected (Table 3): two at St10 (Rains 1 and  
537 2), one at St11 (Rain 3), one at St19 (Rain 4), one during the transit from off Djerba island to  
538 off Zarzis city (Rain 5, south of St19; Fig. 2a, b) (for both collectors), and one at St1 (Rain 6  
539 only in the PAH collector). The “transit to Zarzis” sample was collected as a result of a dry  
540 deposition episode (intense Saharan dust event). In this case, ultra-pure water was used to  
541 rinse the plastic and glass funnels in order to retrieve all the dry fraction that had settled onto  
542 them. Atmospheric samples collected during the cruise were frozen and stored at –20 °C (for  
543 PAHs) or at 4 °C (for metals/metalloids), then filtered (at 0.2 or 0.7 µm) in the laboratory to  
544 separate dissolved and particulate phases before treatments and analyses. Atmospheric  
545 forecast bulletins were regularly sent to the on-board team to anticipate these rain events.  
546 Detailed information on the rain samples collected during the cruise can be found in Table 3.

547 Glass collectors were also set up in two ground stations located in the northern part  
548 (Marseille, France) and southern part (Sfax, Tunisia) of the Mediterranean basin (Fig. 2a; Fig.  
549 S2p) for sampling total (dry and wet) atmospheric deposition and running the subsequent  
550 PAH analyses. This sampling was done on a regular basis (bi-monthly, monthly, or daily in  
551 the case of strong rainfall events) from March 2019 to June 2020, i.e., before, during, and  
552 after the cruise (Poindron et al., in prep.).

#### 553 2.3.11. On-vessel scientific equipment and continuous measurements.

554 Subsurface temperature and salinity were recorded continuously at high frequency all along  
555 the transect from flow-through pumped seawater at 2-m depth, using a thermosalinograph  
556 (TSG, SeaBird SBE 21). A weather station (Batos 1.1 D, Météo France) continuously  
557 recorded atmospheric parameters (temperature, wind, pressure, humidity, PAR).

558

### 559 2.4. The sequence of operations and main parameters analysed on the 560 different size fractions

561 The typical sequence of at-sea/on-board operations conducted from the R/V *Antea* at  
562 each station is given in Table S2. The whole sequence of operations at each station lasted 48 h  
563 on average but varied depending on meteorological conditions encountered and occasional  
564 technical problems. The detailed sequence and timing of the main operations performed  
565 during the whole cruise are presented in Table S3, and the total number of operations  
566 completed is provided Table S4. Table S5 reports the time and depth of sampling (mostly in  
567 the DCM) at each station for the three main operations at sea: the water sampling with the  
568 carousel/Niskin and Go-Flo bottles, *in situ* filtration with the McLane pumps, and plankton  
569 sampling with the MultiNet. Table S6 summarises the main parameters analysed on the  
570 different size fractions (from < 0.2 to > 2000 µm) recovered from filtration and sieving after  
571 the collecting large amounts of plankton, particles, and water in the DCM and

572 surface/subsurface waters (0–5 m depth), i.e., 1) contaminants, with trace metals,  
573 organometals and metalloids (As, Cd, Cr, Cu, Fe, Hg, MeHg, Mn, Ni, Pb, Sb, Zn, etc.),  
574 organic contaminants (PAHs, PCBs, PBDEs, PFASs), radionuclides (<sup>137</sup>Cs) and microplastics,  
575 2) plankton biomass, size structure, taxonomy, cytometry, diversity, and pigment  
576 composition, and 3) biogeochemical parameters, including nutrients [Si(OH)<sub>4</sub>, NO<sub>3</sub><sup>-</sup>, NO<sub>2</sub><sup>-</sup>,  
577 NH<sub>4</sub><sup>+</sup>, PO<sub>4</sub><sup>3-</sup>], TChl<sub>a</sub>, SPM, dissolved and particulate organic matter (POC, PON, DOC,  
578 aCDOM), C and N isotopic ratios (δ<sup>13</sup>C, δ<sup>15</sup>N), and biochemical compounds (carbohydrates,  
579 proteins, lipids).

580

581

### 582 **3. Environmental context during the cruise**

583

#### 584 **3.1. Meteorological context**

585 Atmospheric deposition is known to be an external source of metals and PAHs (Castro-  
586 Jimenez et al., 2012; Jordi et al., 2012; Desboeufs et al., 2022) as well as of nutrients (Guieu  
587 et al., 2020) for Mediterranean surface seawater. The cruise was conducted during the spring,  
588 when dust deposition events were commonplace in the Western Mediterranean (Guieu et al.,  
589 2020). During the cruise, the Aerosol Optical Depth (AOD) maps derived from the Spinning  
590 Enhanced Visible and InfraRed Imager (SEVIRI) satellite instrument ([https://www.icare.univ-  
591 lille.fr/data-access/browse-images/geostationary-satellites/](https://www.icare.univ-<br/>591 lille.fr/data-access/browse-images/geostationary-satellites/); Thieuleux et al., 2005)  
592 highlighted two dust transports with high AOD (> 0.8) through the Mediterranean Sea: one  
593 that occurred between 17 and 26 April 2019 (Fig. 4a; Fig. S6) and a second that occurred  
594 between 3 and 4 May 2019 (Fig. 5a; Fig. S7). These events were associated with significant  
595 cloud cover (Fig. 4b, 5b). The Non-hydrostatic Multiscale Model/Barcelona Supercomputing  
596 Centre (NMMB/BSC)-Dust model and NASCube (<http://nascube.univ-lille1.fr/>; Gonzales and

597 [Briottet, 2017](#)) confirmed the emission and export of dust plumes from North Africa to over  
598 the Western Mediterranean. The atmospheric dynamics and patterns of the first event are  
599 described in detail in [Calidonna et al. \(2020\)](#). This event was associated with a northward  
600 atmospheric flux loaded by dust emission from Algeria and southern Morocco. The second  
601 dust plume was transported from Algeria and Tunisia by north-eastward winds (not shown).

602 For the April event, dust plume transport was mainly associated with wet deposition  
603 from NMMB/BSC-Dust model forecasts, in agreement with the intensely cloudy conditions  
604 ([Fig. 4c, d](#)). The geographic range of dust deposition events covered a region from the  
605 Balearic basin to the Tyrrhenian Sea and then the Ligurian Sea ([Fig. 4a-d](#)), i.e., the vicinity of  
606 R/V's locations during St10 and St11 between 20 and 23 April and then on 25 April along the  
607 Western coastline of Sardinia ([Table 1](#)). The model predictions were confirmed by visual on-  
608 board observations of precipitations around and above the R/V's location, corresponding to  
609 the first three rain samples (Rains 1, 2 and 3) ([Table 3](#)). Note that wet dust deposition started  
610 from the afternoon of 22 April after the R/V's arrival on St10, thus ruling out a direct impact  
611 of dust deposition on the first cast completed at this station. However, rain events probably  
612 impacted surface waters over a large region around the R/V's location during St10 and St11.

613 For the event in May, NMMB/BSC-Dust model forecasts point mainly to dry dust  
614 deposition occurring between 3 and 4 May over the Gulf of Gabès and the Libyan coast ([Fig.](#)  
615 [5c, d](#)). During this event, the R/V was at St19 in the southern Gulf of Gabès then in transit to  
616 Zarzis ([Table 1](#); [Table S3](#)). Dry dust deposition was confirmed by visual observations of  
617 dusty sky and substantial deposited dust material on the decks of the R/V between 3 and 4  
618 May. The Rain 5 sample was collected during this event ([Table 3](#)). The inflow of desert dust  
619 was also consistent with the highest temperatures and lowest pressures recorded by ship's  
620 permanent instrumentation ([Fig. S8](#)). It is therefore very likely that this event represented a  
621 supply of metal-bearing dust to the surface waters.



622 Outside of these desert dust transport periods, Hybrid Single-Particle Lagrangian  
623 Integrated (HYSPLIT) back trajectories modelling showed that the air masses around the R/V  
624 position came from Europe (not shown). Nevertheless, no intense pollution event was either  
625 observed or predicted during the cruise from satellite or model outputs. Moreover, no  
626 volcanic emissions from Etna were recorded during the cruise.

627

### 628 **3.2. Hydrological context**

629 Subsurface (2-m depth) temperature gradually increased from north to south of the  
630 transect, whereas subsurface salinity decreased from North to South but increased again at the  
631 extreme south of the transect (Gulf of Gabès) (Fig. 6). The lowest subsurface temperatures (~  
632 14.0 °C) were recorded in the Bay of Marseille, while the highest subsurface temperatures  
633 (19.5 °C) were observed in the south of the Gulf of Gabès, near Djerba and Zarzis. The  
634 highest subsurface salinity values were found in the Ligurian region (38.5) and the lowest  
635 (37.1) in the northern Tunisian coastal waters, particularly in the Gulf of Tunis (Fig. 2a, 6;  
636 Fig. S1). Because of the vast and contrasted area covered by the cruise, CTD profiles  
637 displayed huge variability with depth in temperature and salinity and in TChla and dissolved  
638 O<sub>2</sub> concentrations between stations (Fig. 7, 8). Despite this high variability, some similarities  
639 emerged. For the stations off French shores (St1–St4), temperature, salinity and TChla values  
640 over the water column ranged from 13.6–14.9 °C, 37.8–38.4 and 0.02–0.86 µg L<sup>-1</sup>,  
641 respectively, with a slight decrease in temperature and a slight increase of salinity towards the  
642 bottom (Fig. 7). Offshore stations (St9–St11) also showed a decrease in temperature and  
643 increase of salinity with depth, but with a greater range of variation (compared to the stations  
644 along the French coast) in terms of temperature (13.4–15.5 °C), salinity (37.3–38.7) and  
645 TChla concentrations (0.00–1.49 µg L<sup>-1</sup>) with manifestly deeper thermoclines and haloclines  
646 (Fig. 7, 8). TChla concentrations were particularly high at St9 (Fig. 7). St11 was marked by a

647 significant increase in both temperature and salinity between 200 and 400 m followed by a  
648 decrease between 400 and 430 m before remaining stable down to the bottom (Fig. 8).  
649 Tunisian stations (St15–St19) showed higher water column temperatures (14.7–17.9 °C) and  
650 lower salinities (37.2–37.8) compared to stations further north, in accordance with subsurface  
651 data (Fig. 6), and lower TChl $a$  concentrations (0.02–0.70  $\mu\text{g L}^{-1}$ ) compared to the  
652 northernmost stations. At these Tunisian stations, thermoclines, haloclines and DCM were  
653 located relatively deep in the water column, although St17 displayed much more  
654 homogeneous profiles (Fig. 8).

655 T–S diagrams allowed us to identify the main water masses encountered at each station  
656 (Fig. 9). At the northern stations (St1–St4) with temperatures of 13.6–14.9 °C and salinities of  
657 37.8–38.4 over 0–150-m depths, we detected (modified) Atlantic Water (AW) coming mainly  
658 from the Ligurian Sea and flowing along the continental slope with Ligurian-Provençal  
659 current. These “resident” AW (RAW), which have been in the Mediterranean for a long time,  
660 have been modified and are saltier (and warmer) than the AW that arrived more recently  
661 through the Strait of Gibraltar (Millot and Taupier-Letage, 2005; Balbín et al., 2014). Moving  
662 south, St9 was characterised by the presence of RAW over the depth 0–300 m and Levantine  
663 Intermediate Water (LIW) over the depth 300–500 m (Fig. 9). LIW is formed in the Eastern  
664 Mediterranean Basin by the combined effect of wintertime cooling and summertime  
665 evaporation, leading to a warm (temperatures of 13.8–16 °C) and salty (salinities of 38.3–39)  
666 intermediate layer that is visible over the whole Mediterranean Sea (Lascaratos et al., 1993;  
667 Balbín et al., 2014; Margirier et al., 2020). Once formed, the LIW spreads throughout the  
668 entire Eastern and Western Basins and can be identified through a salinity maximum at  
669 between ~ 200 and 600-m depth in the Western Basin before it eventually flows out of the  
670 Mediterranean Sea as one of the main components of Mediterranean outflow water (Ben  
671 Ismail et al., 2012; Vargaz-Yanez et al., 2012). In addition, the presence of Western

672 Mediterranean Intermediate Water (WIW) was detected at St9 around 100-m depth with  
673 temperatures of 13.2–13.9 °C and salinities of 38.4–38.6 (Fig. 7, 9). The WIW forms during  
674 winter in the Northwestern Mediterranean Basin due to surface cooling of RAW and  
675 intermediate convection (Salat and Font, 1987; Gasparini et al., 1999) and has been recorded  
676 in the Algerian Basin by Benzohra and Millot (1995) and in the Sicily Channel by Ben Ismail  
677 et al. (2012), flowing eastwards below the AW in the Algerian Current through the Channel  
678 of Sardinia. The WIW is characterised by a relative minimum potential temperature located  
679 between 100 and 200-m depth. The circulation of WIW has only been investigated in the  
680 Algerian Basin, and there is speculation that it follows the same flow paths as the overlying  
681 AW (Millot, 1999). St10 and St11 showed weak signature of the WIW and the presence of  
682 marked LIW indicating a dominant influence of the northward advection of LIW rather than  
683 winter cooling in the water column. The LIW water was well evident in St11, the closest  
684 station to the Sardinia Channel (Fig. 8, 9). At the northernmost tip of the Tunisian coast, the  
685 water temperature progressively increased and the salinity decreased, revealing the presence  
686 of fresher or “new” AW (NAW) coming from the Algerian Basin. The water column arriving  
687 at St15, located in the Gulf of Hammamet, was mostly made up of RAW and NAW with  
688 temperatures of 14.8–17.5 °C and low salinities of 37.1–37.8 from surface to bottom. Moving  
689 southward toward the Gulf of Gabès (GG), the temperature and salinity increased sharply to  
690 reach 17.1 °C and 37.5 at St17 and 17.9 °C and 37.8 at St19 (Fig. 8, 9).

691

### 692 **3.3. Biogeochemical context**

693 The analytical methods used to determine biogeochemical parameters presented in this  
694 section are detailed in Text S1. Considering the whole cruise period, the average (over 32  
695 days) surface TChl $a$  concentration derived from satellite data was higher at St9 (~ 1  $\mu\text{g L}^{-1}$ )  
696 than in the other stations (< 1  $\mu\text{g L}^{-1}$ ) (Fig. 10). The higher content of phytoplankton biomass

697 at St9 was also corroborated in the TChla concentrations actually recorded during the cruise  
698 at 5-m depth, either from CTD measurements or analyses on discrete samples (with a  
699 significant correlation between both measurements:  $r = 0.98$ ,  $n = 10$ ,  $p < 0.0001$ ; [Table S7](#)). In  
700 line with the discrete samples, the highest TChla concentrations at 5-m depth were found at  
701 St9 ( $2.90 \mu\text{g L}^{-1}$ ) followed by St4 ( $1.57 \mu\text{g L}^{-1}$ ) and St1 ( $0.84 \mu\text{g L}^{-1}$ ), while the lowest TChla  
702 concentrations were observed at St17 ( $0.15 \mu\text{g L}^{-1}$ ) and St15 ( $0.10 \mu\text{g L}^{-1}$ ) ([Table S7](#)).

703 DCM was shallowest at St4 (13 m), St1 and St9 (20 m) and deepest at St10 (51 m), St2,  
704 St3 (53 m) and St15 (66 m) ([Fig. 7, 8, 11a](#); [Table S7](#)). TChla in the DCM followed a fairly  
705 similar pattern of distribution to TChla at 5-m depth, with a significant correlation between  
706 both measures based on both CTD and discrete sample data ( $r = 0.64\text{--}0.92$ ,  $n = 10$ ,  $p =$   
707  $0.0001\text{--}0.048$ ). TChla concentrations measured on discrete samples from the DCM were  
708 highest at St9 ( $1.54 \mu\text{g L}^{-1}$ ), in line with the surface/subsurface TChla data ([Fig. 10](#)). High  
709 TChla concentrations were also recorded south of the Gulf of Gabès (at St19:  $1.45 \mu\text{g L}^{-1}$ )  
710 ([Fig. 11b](#); [Table S7](#)), even though at this station it was not really a DCM that was observed  
711 but rather a bottom-lying bead, as can often be observed for shallow coastal stations. St4 and  
712 St1 showed fairly high TChla concentrations of  $0.98$  and  $0.77 \mu\text{g L}^{-1}$ , respectively. The lowest  
713 TChla concentrations in the DCM were found at St17 ( $0.21 \mu\text{g L}^{-1}$ ), St2, and St11 ( $0.38 \mu\text{g L}^{-1}$ )  
714 ([Fig. 11b](#); [Table S7](#)).

715 The North-to-South distribution of other biogeochemical parameters measured in the  
716 DCM presented interesting features. POC concentration had a fairly similar pattern of  
717 distribution to TChla, with decreasing values from St1 to St3, a maximal value at St9 ( $156.4$   
718  $\mu\text{g L}^{-1}$ ), then a decrease up to St17, and finally a higher value at St19 ( $55.9 \mu\text{g L}^{-1}$ ) ([Fig. 11c](#);  
719 [Table S7](#)).  $\text{Si(OH)}_4$  concentration followed much the same pattern but with an increase from  
720 St1 to St3 and a maximal value at both St9 and St19 ( $\sim 2.00 \mu\text{M}$ ) ([Fig. 11d](#); [Table S7](#)).  $\text{NO}_3^-$   
721 concentration increased from St1 to its peak at St3 ( $1.31 \mu\text{M}$ ), was still high at St9 ( $0.96 \mu\text{M}$ ),

722 and then decreased along to St17–St19 (Fig. 11e; Table S7).  $\text{PO}_4^{3-}$  concentration was  
723 particularly high at St3 (0.31  $\mu\text{M}$ ) and St19 (0.55  $\mu\text{M}$ ) (Fig. 11f; Table S7). Finally, DOC  
724 concentration and  $a_{\text{CDOM}}$  decreased from St1 to St9 or St10 then increased up to St19 where  
725 they reached maximal values (76.2  $\mu\text{M}$  and 2.05  $\text{m}^{-1}$ , respectively) (Fig. 11g, h; Table S7).

726 Principal component analysis (PCA) based on the Pearson's correlation matrix was  
727 applied on these biogeochemical parameters recorded in the DCM at each station (Fig. 12).  
728 The first principal component (PC1), which explained 47% of total variance within samples,  
729 was mainly driven by  $\text{PO}_4^{3-}$ , DOC,  $a_{\text{CDOM}}$ , and to a lesser extent TChla and  $\text{Si}(\text{OH})_4$ . The  
730 second principal component (PC2), which accounted for 34% of total variance, was driven by  
731 POC,  $\text{NO}_3^-$ , TChla, and  $\text{Si}(\text{OH})_4$ . Four groups of samples (stations) emerged from this PCA:  
732 1) St2, St3, St4, St10, characterised by moderate concentrations of nutrients and TChla and a  
733 low organic matter content; 2) St1, St11, St15, St17, with the lowest concentrations in  
734 nutrients and TChla (except St1); 3) St9, which showed the highest in  $\text{Si}(\text{OH})_4$ ,  $\text{NO}_3^-$ , TChla  
735 and POC concentrations, and the lowest  $\text{PO}_4^{3-}$  and DOM contents; 4) St19, which showed the  
736 highest concentrations in  $\text{Si}(\text{OH})_4$ , TChla (equivalent to those of St9),  $\text{PO}_4^{3-}$  and DOM as well  
737 as high POC and low  $\text{NO}_3^-$  concentrations (Fig. 12).

738 Overall, the levels of TChla, nutrients and other biogeochemical parameters observed  
739 along the North-South transect in the subsurface waters and DCM in spring 2019 during the  
740 MERITE-HIPPOCAMPE cruise are consistent with previous observations in the  
741 Mediterranean Sea (The Mermex Group, 2011; Salgado-Hernanz et al., 2019; Guieu et al.,  
742 2020; Marañón et al., 2021). The TChla levels in the different stations were also consistent  
743 with their positioning in terms of bloom-condition areas and consensus regions defined by  
744 D'Ortenzio and d'Alcalà (2009) and Ayata et al. (2018). TChla concentrations tended to be  
745 higher at stations located north of the North Balearic front (St1–St4, St9) than stations located  
746 south (St10, St11, St15, St17, St19).

747 Interestingly, two stations, St9 and St19, clearly stood apart from the others in terms of  
748 biogeochemical content (Fig. 11, 12). St9 was situated at the boundary of the Ligurian  
749 consensus region, in the wintertime deep convection area. Time-series of water temperature  
750 recorded at different depths at the LION mooring (42° 02' N, 4° 40' E) highlighted a  
751 deepening of the mixed layer depth and thus the convection process down to 1500-m depth  
752 within the Ligurian area in early February 2019 (Fig. S9). In late March 2019, the end of the  
753 convection process induced the occurrence of an intense phytoplankton bloom in the same  
754 area (Fig. S9). This illustrates the fact that 2019 was a relatively convective and productive  
755 year (Margirier et al., 2020; Bosse et al., 2022), and that St9, located at the border of this  
756 convective and productive zone, still presented high concentrations of TChla, POC and some  
757 nutrients in the May 2019 sampling period.

758 The high levels of TChla, Si(OH)<sub>4</sub>, PO<sub>4</sub><sup>3-</sup>, DOM, and POC encountered at St19 south of  
759 the Gulf of Gabès is probably related to the Saharan dust deposition event (see section 3.1),  
760 but the effect of sediment resuspension cannot be excluded due to high wind speeds during  
761 this period (Fig. S8). In the Gulf of Gabès, TChla concentrations can reach > 1 µg L<sup>-1</sup> close to  
762 the coast of Djerba and Kerkennah Islands during the spring season (Bel Hassen et al., 2009).  
763 The Gulf of Gabès is known to be regularly submitted to Saharan dust deposition (Béjaoui et  
764 al., 2019). This Saharan dust, enriched in phosphorus, has been shown to induce  
765 phytoplankton blooms in the Gulf (Hamza et al., 2016; Béjaoui et al., 2019), and as described  
766 above, intense Saharan dust deposition events occurred in this area during the cruise, for  
767 which we collected on-board rain and particle samples (Table 3; Fig. 5; Fig. S7, S8).  
768 Furthermore, in this shallow ecosystem submitted to strong tides and resulting currents,  
769 disturbance and resuspension of sediments could release elements such as nutrients and  
770 organic matter into the water column, which in turn may stimulate planktonic activity (Bel  
771 Hassen et al., 2009; Fourati et al., 2018; Zouch et al., 2018).

772

773

#### 774 **4. Overview of the types of articles produced through the cruise**

775

776 [Fig. 13](#) shows the types of articles that are a part of this special issue in the frame of the  
777 MERITE-HIPPOCAMPE cruise. There are a series of articles concerning the transfer and  
778 accumulation of contaminants in planktonic food webs in the DCM but also in  
779 surface/subsurface waters. These articles present: 1) contaminant concentrations in the  
780 different planktonic/particulate size fractions and, for several of them, in the dissolved phase  
781 of water (see [Table S6](#) for the size fractions–contaminant analysis correspondence), and 2)  
782 their resulting factors of bioconcentration, bioaccumulation or food accumulation. The  
783 contaminants investigated are trace metals/metalloids (Cr, Mn, Fe, Co, Ni, Cu, Zn, As, Se,  
784 Mo, Ag, Cd, Sb, Pb...) ([Chifflet et al., 2023](#)), with a focus on Cu and Zn isotopes ([Chifflet et  
785 al., 2022](#)), Hg and MeHg ([Tesán Onrubia et al., in prep.](#)), PAHs ([Guigue et al., in prep.](#)),  
786 PCBs, PBDEs, PFASs ([Tronczynski et al., in prep.](#)), and radionuclides ( $^{137}\text{Cs}$ ) ([Radakovitch  
787 et al., in prep.](#)). Another work will treat of the abundance and composition of microplastics in  
788 both surface waters and the DCM ([Fig. 13](#)).

789 There are also a series of articles dealing with the composition and structure of  
790 planktonic food webs. Indeed, the paper by [Tesán Onrubia et al. \(2023\)](#) on the stable C and N  
791 isotopes ( $\delta^{13}\text{C}$ ,  $\delta^{15}\text{N}$ ) and biochemical content (lipids, carbohydrates, proteins) of the different  
792 planktonic size fractions serves to highlight the structure of planktonic food webs and the  
793 transfer of organic matter within them, and to assess the factors of trophic accumulation used  
794 in the contaminant-related papers. Moreover, several articles use the cytometry and  
795 taxonomy/microscope analyses, imaging (zooscan, flowcam), optical *in situ* measurements  
796 (LOPC, LISST-HOLO) and/or 16S and 18S rRNA high-throughput sequencing analyses to

797 cover the abundance, biomass, distribution, size structure, and composition/diversity of the  
798 following planktonic groups, mostly for the DCM but also for surface/subsurface waters or  
799 even within the 0–200-m depth layer (see [Table S6](#) for the correspondence with size  
800 fractions): pico-, nano- and micro-phytoplankton ([Boudriga et al., 2022](#); [Bellaaj Zouari et al.,](#)  
801 [in prep.](#)), micro- and meso-zooplankton and their biomass ratio with detritus ([Fierro-González](#)  
802 [et al., 2023](#)), as well as free-living and plankton-associated bacterioplankton (heterotrophic  
803 prokaryotes) ([Bellaaj Zouari et al., in prep.](#); [Quéméneur et al., in prep.](#)), and nano- and micro-  
804 zooplankton related to the microbial loop ([Bellaaj Zouari et al., in prep.](#)). In addition, a  
805 complementary paper proposes a methodological approach for the study of the microbiota  
806 associated with plankton ([Cabrol et al., in prep.](#)). Also, the effect of the Saharan dust  
807 deposition event on pico- and nano-phytoplankton community in the south of Gabès is  
808 covered by [Boudriga et al. \(in prep.\)](#). Overall, these articles will allow us to understand which  
809 planktonic groups are present and how they influence/participate in transfers of contaminants  
810 within planktonic networks. Our understanding of the contaminant transfer processes at work  
811 within planktonic food webs is also enhanced by the dilution experiments and the subsequent  
812 determination of phytoplankton production rates and micro- and meso-zooplankton grazing  
813 rates ([Meddeb et al., in prep.](#)) ([Fig. 13](#)), as well as the grazing and excretion rates estimated  
814 from the zooplankton size-structure according to allometric relationships allowing an  
815 estimation of grazing pressure and nutrient recycling by the metazooplankton ([Fierro-](#)  
816 [González et al., 2023](#)).

817 Looking beyond plankton, there is one article dedicated to  $\delta^{13}\text{C}$  and  $\delta^{15}\text{N}$  stable isotopes  
818 and concentrations of Hg, PAHs and PCBs in small pelagic fishes collected in Tunisian  
819 waters ([Lajnef et al., in prep.](#)). This study should provide valuable pointers to help establish a  
820 link between the contamination of plankton and the contamination of higher trophic levels.  
821 The concentrations of trace metals and PAHs in wet (rain) atmospheric deposition samples



822 collected during the cruise and on land is investigated to assess the role of dry/wet  
823 atmospheric deposition as a source of contaminants in surface marine waters (Poindron et al.,  
824 in prep.). Finally, the overall transport patterns and hydrodynamic context of the cruise using  
825 modelling and satellite data, and their potential implication for contaminant origin and  
826 distribution are addressed by Rwawi et al. (in prep.) (Fig. 13).

827

828

### 829 **Data availability**

830 All data from the MERITE-HIPPOCAMPE cruise (<https://doi.org/10.17600/18000900>;  
831 Tedetti and Tronczynski, 2019) is stored in the MISTRALS-SEDOO database  
832 (<https://mistrals.sedoo.fr/MERITE/>) and will be made publicly accessible once all the articles  
833 related to the cruise are published in the present special issue. In the meantime, data can be  
834 obtained upon request from the corresponding author. In addition, navigation data and CTD  
835 profiles from the MERITE-HIPPOCAMPE cruise are available *via* the IFREMER/SISMER  
836 database (<https://data.ifremer.fr/SISMER>).

837

838

### 839 **Author contribution statement**

840 All the authors participated in the MERITE-HIPPOCAMPE project and design of the  
841 manuscript.

842 *Conception and design of study:* M.T., J.T., F.C., M.P., S.B.I., C.S., M.B.H., K.D.,  
843 S.C., A.B.Z., D.B., A.B., C.B.-P., N.B., L.C., C.C., L.C., M.N.D.Y., A.D., J.-C.D., C.G.,  
844 L.G., A.H., L.-E.H.-B., S.J., J.K., B.M., O.P., M.Q., O.R., A.S.H., M.T., N.Z., C.G.

845 *Acquisition of data:* M.T., J.T., F.C., M.P., S.B.I., M.B.H., K.D., S.C., A.B.Z., M.A.,  
846 S.A., L.B.A., N.B., I.B., A.B., N.B., L.C., T. de G.-T., M.F., F.G., L.G., J.K., N.M.B., D.M.,  
847 J.-C.M., M.M., M.Q., O.R., C.R., A.S.H., J.A.T.O., B.T., M.T., N.Z.

848 *Analysis and/or interpretation of data:* M.T., J.T., F.C., M.P., S.B.I., M M.B.H., K.D.,  
849 C.P., S.C., A.B.Z., S.A., D.B., L.B.A, I.B., A.B., C.B.-P., N.B., L.C., C.C., L.C., S.C., A.D.,  
850 B.E., P.F.-G., N.G., F.G., C.G., L.G., A.H., L.-E.H.-B., S.J., J.K., R.L., N.M.B, P.L.M., A.B.,  
851 M.M., B.M., M.Q., O.R., P.R., V.R., C.R., A.S.H., J.A.T.O., B.T., M.T., N.Z.

852 *Drafting the manuscript:* M.T., J.T., F.C., M.P., S.B.I., K.D., C.P., S.C., P.L.M., A.B.

853 *Revising/editing the manuscript:* J.T., F.C., M.P., C.S., M.B.H., K.D., C.P., A.B.Z.,  
854 M.A., S.A., D.B., L.B.A., N.B., I.B., A.B., C.B.-P., N.B., L.C., C.C., L.C., S.C., M.N.D.Y., T.  
855 de G.-T., A.D., J.-C.D., B.E., P.F.-G., M.F., N.G., F.G., C.G., L.G., A.H., L.-E.H.-B., S.J.,  
856 J.K., R.L., N.M.B., D.M., A.B., J.-C.M., M.M., B.M., O.P., M.Q., O.R., P.R., C.R., V.R.,  
857 C.R., A.S.H., J.A.T.O., B.T., M.T., N.Z.

858 *Project administration and funding acquisition:* M.T., J.T., F.C., M.P., K.D., C.S.

859

860

## 861 **Acknowledgments**

862 The MERITE-HIPPOCAMPE project was initiated and funded by the cross-disciplinary  
863 *Pollution & Contaminants* axis of the CNRS-INSU MISTRALS program (joint action of the  
864 MERMEX-MERITE and CHARMEX subprograms). The project also received financial  
865 support from the IRD French-Tunisian International Joint Laboratory (LMI) COSYS-Med.  
866 The MERITE-HIPPOCAMPE cruise was organised and supported by the French  
867 Oceanographic Fleet (FOF), CNRS/INSU, IFREMER, IRD, the Tunisian Ministry of  
868 Agriculture, Water Resources and Fisheries, and the Tunisian Ministry of Higher Education  
869 and Scientific Research. The project also benefited from additional funding by IFREMER, by

870 the MIO Action Sud and Transverse Axis programs (CONTAM Transverse Axis), by the IRD  
871 Ocean Department, and by the CONTAMPUMP project, funded by the French National  
872 Research Agency (ANR) (ANR JCJC #19-CE34-0001-01). It was also supported by the  
873 Chemical and Physical Properties of the Atmosphere (CaPPA) project, funded by the ANR  
874 through the Programme d'Investissement d'Avenir (PIA) under contract ANR-11-LABX-  
875 0005-01, and by the Regional Council Nord-Pas de Calais and the European Funds for  
876 Regional Economic Development (FEDER). We are grateful to the captains and crew of the  
877 R/V *Antea* for their help and assistance during the cruise, as well as to the captain and crew of  
878 the R/V *Hannibal* (INSTM, Tunisia) for sampling small pelagic fishes in the Tunisian waters.  
879 We also thank the captain and crew of the R/V *Antédon 2* for the pre-HIPPOCAMPE cruise  
880 performed in the Bay of Marseille in 2018. IFREMER-FOF and Genavir teams provided  
881 valuable technical and administrative support for the preparation and conduct of the cruise.  
882 We warmly thank P. Vert, F. André and A. Miere from Observatoire Midi-Pyrénées/SEDOO  
883 for the implementation of the HIPPOCAMPE Operation Centre (<http://hippoc.sedoo.fr/>) and  
884 the MERITE-HIPPOCAMPE database (<https://mistrals.sedoo.fr/MERITE/>). We also thank F.  
885 Dulac (LSCE) for his contribution in the early phases of the project. We thank E. de Saint-  
886 Léger and F. Perault (DT-INSU, Brest) for provisioning the *in situ* McLane pumps with  
887 sequential filtration units, and A. Smirnov (NASA Goddard Space Flight Centre) for  
888 provisioning the Microtops sunphotometer. The IRD's representation in Tunisia, the French  
889 Institute of Tunisia, and INSTM provided valuable logistics and/or financial assistance to help  
890 prepare the cruise, and CNRS-INSU, IFREMER, IRD, IRSN and MIO communications and  
891 outreach divisions helped promote the campaign. We are grateful to the Station Marine  
892 d'Endoume (OSU Institut Pythéas, Aix-Marseille Université, CNRS) and to the INSTM for  
893 providing the facilities to host the atmospheric deposition collectors in Marseille and Sfax.  
894 We thank L. Casalot (MIO) and the IRD for helpful support on implementing the "Accès et

895 partage des avantages découlant de l'utilisation des ressources génétiques et des  
896 connaissances traditionnelles associées" (APA) procedure. Various MIO platforms also  
897 provided valuable support: the Service Atmosphère-Mer (SAM), for preparation and  
898 management of the embarked material, the Plateforme Analytique de Chimie des  
899 Environnements Marins (PACEM platform) for various chemical analyses, the Platform  
900 Microscopie et Imagerie (MIM platform) for plankton analyses, and the Plateforme Régionale  
901 de Cytométrie pour la Microbiologie (PRECYM platform) for cytometric analyses. L.  
902 Gouriou (IFREMER, LER-AR Arcachon) ran HPLC analyses of the pigments. I. Fronval and  
903 V. Riffault (IMT NE) performed the analyses of PAHs in atmospheric deposition and  
904 contributed to data interpretation. We used imagery taken from the NASA Worldview  
905 application (<https://worldview.earthdata.nasa.gov>), which is part of the NASA Earth  
906 Observing System Data and Information System (EOSDIS). Data and/or images from the  
907 NMMB/BSC-Dust or BSC-DREAM8b model were produced by the Barcelona  
908 Supercomputing Centre (<http://www.bsc.es/ess/bsc-dust-daily-forecast/>). The average surface  
909 Chla image was obtained from EU Copernicus Marine Service Information (CMEMS;  
910 <https://marine.copernicus.eu/>). This paper and special issue are dedicated to our friend and  
911 colleague, Cédric Garnier, who passed away in 2018. Cédric was a deeply-involved and very  
912 active member of the MERMEX-MERITE program, and was part of the team that initiated  
913 and promoted the MERITE-HIPPOCAMPE cruise project. Finally, we are grateful to two  
914 anonymous reviewers for their helpful and constructive comments and corrections.

915

916

### 917 **Supplementary information**

918       Supplementary material related to this article is available online at: xxx

919

920 **References**

- 921 Alcaraz, M., Calbet, A., 2003. Zooplankton Ecology. *Marine Ecology*, pp. 16.
- 922 Alekseenko, E., Thouvenin, B., Tronczyński, J., Carlotti, F., Garreau, P., Tixier, C., Baklouti,  
923 M., 2018. Modeling of PCB trophic transfer in the Gulf of Lions; 3D coupled model  
924 application. *Marine Pollution Bulletin*, 128, 140–155. doi:  
925 10.1016/j.marpolbul.2018.01.008
- 926 Ayata, S.D., Irisson, J.O., Aubert, A., Berline, L., Dutay, J.C., Mayot, N., Nieblas, A.E.,  
927 D’Ortenzio, F., Palmieri, J., Reygondeau, G., Rossi, V., Guieu, C., 2018. Regionalisation  
928 of the Mediterranean basin, a MERMEX synthesis. *Progress in Oceanography*, 163, 7–20.  
929 doi: 10.1016/j.pocean.2017.09.016
- 930 Balbín, R., López-Jurado, J., Flexas, M., Reglero, P., Vélez-Velchí, P., González-Pola, C.,  
931 Rodríguez, J., García, A., Alemany, F., 2014. Interannual variability of the early summer  
932 circulation around the balearic islands: Driving factors and potential effects on the marine  
933 ecosystem. *Journal of Marine Systems*, 138, 70–81. doi: 10.1016/j.jmarsys.2013.07.004
- 934 Barhoumi, B., Castro-Jiménez, J., Guigue, C., Goutx, M., Sempéré, R., Derouiche, A.,  
935 Achour, A., Touil, S., Driss, M.R., Tedetti, M., 2018. Levels and risk assessment of  
936 hydrocarbons and organochlorines in aerosols from a north African coastal city (Bizerte,  
937 Tunisia). *Environmental Pollution*, 240, 422–431. doi: 10.1016/j.envpol.2018.04.109
- 938 Barral, Q.B., Zakardjian, B., Dumas, F., Garreau, P., Testor, P., Beuvier, J., 2021.  
939 Characterization of fronts in the Western Mediterranean with a special focus on the North  
940 Balearic Front. *Progress in Oceanography*, 197, 102636. doi:  
941 10.1016/j.pocean.2021.102636
- 942 Barrier, N., Petrenko, A.A., Ourmières, Y., 2016. Strong intrusions of the Northern  
943 Mediterranean Current on the eastern Gulf of Lion: insights from in-situ observations and

944 high resolution numerical modelling. *Ocean Dynamics*, 66, 313–327. doi: 10.1007/s10236-  
945 016-0921-7

946 Béjaoui, B., Ben Ismail, S., Othmani, A., Ben Abdallah-Ben Hadj Hamida, O., Chevalier, C.,  
947 Feki-Sahnoun, W., Harzallah, A., Ben Hadj Hamida, N., Bouaziz, R., Dahech, S., Diaz, F.,  
948 Tounsi, K., Sammari, C., Pagano, M., Bel Hassen, M., 2019. Synthesis review of the Gulf  
949 of Gabes (eastern Mediterranean Sea, Tunisia): morphological, climatic, physical  
950 oceanographic, biogeochemical and fisheries features. *Estuarine, Coastal and Shelf  
951 Science*, 219, 395–408. doi: 10.1016/j.ecss.2019.01.006

952 Bel Hassen, M., Hamza, A., Drira, Z., Zouari, A., Akrouf, F., Messaoudi, S., Aleya, L.,  
953 Ayadi, H., 2009. Phytoplankton-pigment signatures and their relationship to spring  
954 summer stratification in the Gulf of Gabes. *Estuarine, Coastal and Shelf Science*, 83, 296–  
955 306. doi: 10.1016/j.ecss.2009.04.002

956 Ben Ismail, S., Sammari, C., Gasparini, G.P., Béranger, K., Brahim, M., Aleya, L., 2012.  
957 Water masses exchanged through the Channel of Sicily: evidence for the presence of new  
958 water masses on the Tunisian side of the Channel. *Deep Sea Research Part I*, 63, 65–81.  
959 doi: 10.1016/j.dsr.2011.12.009

960 Benzohra, M., Millot, C., 1995. Characteristics and circulation of the surface and intermediate  
961 water masses off Algeria. *Deep-Sea Research Part I*, 42, 1803–1830. doi: 10.1016/0967-  
962 0637(95)00043-6

963 Berline, L., Rammou, A., Doglioli, A., Molcard, A., Petrenko, A., 2014. A connectivity based  
964 ecoregionalization of the Mediterranean Sea. *PLoS ONE*, 9, e111978. doi:  
965 10.1371/journal.pone.0111978

966 Berrojalbiz, N., Dachs, J., Ojeda, M.J., Valle, M.C., Castro-Jimenez, J., Wollgast, J., Ghiani,  
967 M., Hanke, G., Zaldivar, J.M., 2011. Biogeochemical and physical controls on  
968 concentrations of polycyclic aromatic hydrocarbons in water and plankton of the

969 Mediterranean and Black Seas. *Global Biogeochemical Cycles*, 25, GB4003.  
970 doi:10.1029/2010GB003775, 2011

971 Bishop, J.K.B., Lam, P.J., Wood, T.J., 2012. Getting good particles: Accurate sampling of  
972 particles by large volume in-situ filtration. *Limnology and Oceanography: Methods*, 10,  
973 681–710. doi: 10.4319/lom.2012.10.681

974 Bishop, J.K.B., Wood, T.J., 2008. Particulate matter chemistry and dynamics in the twilight  
975 zone at VERTIGO ALOHA and K2 sites. *Deep Sea Research I*, 55, 1684–1706. doi:  
976 10.1016/j.dsr.2008.07.012

977 Bodiguel, X., Loizeau, V., Le Guellec, A.-M., Roupsard, F., Philippon, X., Mellon-Duval, C.,  
978 2009. Influence of sex, maturity and reproduction on PCB and p,p'DDE concentrations and  
979 repartitions in the European hake (*Merluccius merluccius*, L.) from the Gulf of Lions  
980 (N.W. Mediterranean). *Science of the Total Environment*, 408, 304–311. doi:  
981 10.1016/j.scitotenv.2009.10.004

982 Bosse, A., Testor, P., Coppola L., Bretel, P., Dausse, D., Durrieu de Madron, X., Houpert, L.,  
983 Labaste, M., Legoff, H., Mortier, L., D'Ortenzio, F., 2022. LION observatory data.  
984 SEANOE. doi: 10.17882/44411

985 Boudriga, I., Thyssen, M., Zouari, A., Garcia, N., Tedetti, M., Bel Hassen, M., 2022.  
986 Ultraphytoplankton community structure in subsurface waters along a North-South  
987 Mediterranean transect. *Marine Pollution Bulletin*, 182, 113977. doi:  
988 [10.1016/j.marpolbul.2022.113977](https://doi.org/10.1016/j.marpolbul.2022.113977)

989 Calidonna, C.R., Avolio, E., Gullì, D., Ammoscato, I., De Pino, M., Donateo, A., Lo Feudo,  
990 T., 2020. Five Years of Dust Episodes at the Southern Italy GAW Regional Coastal  
991 Mediterranean Observatory: Multisensors and Modeling Analysis. *Atmosphere*, 11, 456.  
992 doi: 10.3390/atmos11050456

993 Casal, P., González-Gaya, B., Zhang, Y., Reardon, A.J.F., Martin, J.W., Jiménez, B., Dachs,  
994 J., 2017. Accumulation of perfluoroalkylated substances in oceanic plankton.  
995 *Environmental Science and Technology*, 51, 2766–2775. doi: 10.1021/acs.est.6b05821

996 Castro-Jiménez, J., Bănaru, D., Chen, C.-T., Jiménez, B., Muñoz-Arnanz, J., Deviller, G.,  
997 Sempéré, R., 2021. Persistent organic pollutants burden, trophic magnification and risk in a  
998 pelagic food web from coastal NW Mediterranean Sea. *Environmental Science and*  
999 *Technology*, 55, 9557–9568. doi: 10.1021/acs.est.1c00904

1000 Castro-Jiménez, J., Barhoumi, B., Paluselli, A., Tedetti, M., Jiménez, B., Muñoz-Arnanz, J.,  
1001 Wortham, H., Driss, M.R., Sempéré, R., 2017. Occurrence, loading and exposure of  
1002 atmospheric particle-bound POPs at the African and European edges of the western  
1003 Mediterranean Sea. *Environmental Science and Technology*, 51, 13180–13189. doi:  
1004 10.1021/acs.est.7b04614

1005 Castro-Jiménez, J., Berrojalbiz, N., Wollgast, J., Dachs, J., 2012. Polycyclic aromatic  
1006 hydrocarbons (PAHs) in the Mediterranean Sea: Atmospheric occurrence, deposition and  
1007 decoupling with settling fluxes in the water column. *Environmental Pollution*, 166, 40–47.  
1008 doi: 10.1016/j.envpol.2012.03.003

1009 Chifflet, S., Briant, N., Freydier, R., Araújo, D.F., Quéméneur, M., Zouch, H., Bellaaj-Zouari,  
1010 A., Carlotti, F., Tedetti, M., 2022. Isotopic compositions of copper and zinc in plankton  
1011 from the Mediterranean Sea (MERITE-HIPPOCAMPE campaign): Tracing trophic  
1012 transfer and geogenic inputs. *Marine Pollution Bulletin*, 185, 114315. doi:  
1013 10.1016/j.marpolbul.2022.114315

1014 Chifflet, S., Briant, N., Tesán-Onrubia, J.A., Zaaboub, N., Amri, S., Radakovitch, O., Bănaru,  
1015 D., Tedetti, M., 2023. Distribution and accumulation of metals and metalloids in  
1016 planktonic food webs of the Mediterranean Sea (MERITE-HIPPOCAMPE campaign).  
1017 *Marine Pollution Bulletin*, 186, 114384. doi: 10.1016/j.marpolbul.2022.114384



1018 Chouvelon, T., Cresson, P., Bouchoucha, M., Brach-Papa, C., Bustamante, P., Crochet, S.,  
1019 Marco-Miralles, F., Thomas, B., Knoery, J., 2018. Oligotrophy as a major driver of  
1020 mercury bioaccumulation in medium-to high-trophic level consumers: a marine ecosystem-  
1021 comparative study. *Environmental Pollution*, 233, 844–854. doi:  
1022 10.1016/j.envpol.2017.11.015

1023 Chouvelon, T., Strady, E., Harmelin-Vivien, M., Radakovitch, O., Brach-Papa, C., Crochet,  
1024 S., Knoery, J., Rozuel, E., Thomas, B., Tronczynski, J., Chiffolleau, J.F., 2019. Patterns of  
1025 trace metal bioaccumulation and trophic transfer in a phytoplankton-zooplankton-small  
1026 pelagic fish marine food web, *Marine Pollution Bulletin*, 146, 1013–1030. doi:  
1027 10.1016/j.marpolbul.2019.07.047

1028 Cossa, D., Coquery, M., 2005. The Mediterranean mercury anomaly, a geochemical or a  
1029 biological issue. In: Saliot, A. (Ed.), *The Mediterranean Sea. Handbook of Environmental*  
1030 *Chemistry*, pp. 177–208

1031 Cossa, D., Knoery, J., Bănar, D., Harmelin-Vivien, M., Sonke, J.E., Hedgecock, I.M., Bravo,  
1032 A.G., Rosati, G., Canu, D., Horvat, M., Sprovieri, F., Pirrone, N., Heimbürger-Boavida,  
1033 L.E., 2022. Mediterranean Mercury Assessment 2022: An Updated Budget, Health  
1034 Consequences, and Research Perspectives. *Environmental Science and Technology*, 56,  
1035 3840–3862. doi: 10.1021/acs.est.1c03044

1036 D’Ortenzio, F., d’Alcalà, M.R., 2009. On the trophic regimes of the Mediterranean Sea: a  
1037 satellite analysis. *Biogeosciences*, 6, 139–148. doi: 10.5194/bg-6-139-2009

1038 Dachs, J., Lohmann, R., Ockenden, W.A., Mejanelle, L., Eisenreich, S.J., Jones, K.C., 2002.  
1039 Oceanic biogeochemical controls on global dynamics of persistent organic pollutants.  
1040 *Environmental Science and Technology*, 36, 4229–4237. doi: 10.1021/es025724k

1041 Dachs, J., Méjanelle, L., 2010. Organic Pollutants in Coastal Waters, Sediments, and Biota: A  
1042 Relevant Driver for Ecosystems During the Anthropocene? *Estuaries and Coasts*, 33, 1–14.  
1043 doi: 10.1007/s12237-009-9255-8

1044 Desboeufs, K., Fu, F., Bressac, M., Tovar-Sánchez, A., Triquet, S., Doussin, J.-F., Giorio, C.,  
1045 Chazette, P., Disnaquet, J., Feron, A., Formenti, P., Maisonneuve, F., Rodríguez-Romero,  
1046 A., Zapf, P., Dulac, F., Guieu, C., 2022. Wet deposition in the remote western and central  
1047 Mediterranean as a source of trace metals to surface seawater. *Atmospheric Chemistry and*  
1048 *Physics*, 22, 2309–2332, <https://doi.org/10.5194/acp-22-2309-2022>.

1049 Ding, Q., Gong, X., Jin, M., Yao, X., Zhang, L., Zhao, Z., 2021. The biological pump effects  
1050 of phytoplankton on the occurrence and benthic bioaccumulation of hydrophobic organic  
1051 contaminants (HOCs) in a hypereutrophic lake. *Ecotoxicology and Environmental Safety*,  
1052 213, 112017. doi: 10.1016/j.ecoenv.2021.112017

1053 Duran, R., Cravo-Laureau, C., 2016. Role of environmental factors and microorganisms in  
1054 determining the fate of polycyclic aromatic hydrocarbons in the marine environment.  
1055 *FEMS Microbiology Reviews*, 40, 814–830. doi: 10.1093/femsre/fuw031

1056 El Hourany, R., Abboud-Abi Saab, M., Faour, G., Mejia, C., Crépon, M., Thiria, S., 2019.  
1057 Phytoplankton diversity in the Mediterranean Sea from satellite data using self-organizing  
1058 maps. *Journal of Geophysical Research Oceans*, 124, 5827–5843. doi:  
1059 10.1029/2019JC015131

1060 Elbaz-Poulichet, F., Morley, N.H., Beckers, J.-M., Nomerange, P., 2001. Metal fluxes through  
1061 the Strait of Gibraltar: the influence of the Tinto and Odiel rivers (SW Spain). *Marine*  
1062 *Chemistry*, 73, 93–213. doi: 10.1016/S0304-4203(00)00106-7

1063 Everaert, G., De Laender, F., Goethals, P.L.M., Janssen, C.R., 2015. Multidecadal field data  
1064 Support intimate links between phytoplankton dynamics and PCB concentrations in marine

1065 sediments and biota. *Environmental Sciences and Technology*, 49, 8704–8711. doi:  
1066 10.1021/acs.est.5b01159

1067 Fan, C.-W., Reinfelder, J.R., 2003. Phenanthrene Accumulation Kinetics in Marine Diatoms.  
1068 *Environmental Science and Technology*, 37, 3405–3412. doi: 10.1021/es026367g

1069 Fierro-González, P., Pagano, M., Guilloux, L., Makhoulouf Belkahia, N., Tedetti, M., Carlotti,  
1070 F., 2023. Zooplankton biomass, size structure, and associated metabolic fluxes with focus  
1071 on its roles at the chlorophyll maximum layer during the plankton-contaminant MERITE-  
1072 HIPPOCAMPE cruise. Submitted to this special issue.

1073 Fourati, R., Tedetti, M., Guigue, C., Goutx, M., Garcia, N., Zaghden, H., Sayadi, S., Elleuch,  
1074 B., 2018. Sources and spatial distribution of dissolved aliphatic and polycyclic aromatic  
1075 hydrocarbons in surface coastal waters from the Gulf of Gabès (Tunisia, Southern  
1076 Mediterranean Sea). *Progress in Oceanography*, 163, 232–247. doi:  
1077 10.1016/j.pocean.2017.02.001

1078 Frouin, H., Dangerfield, N., Macdonald, R.W., Galbraith, M., Crewe, N., Shaw, P., Mackas,  
1079 D., Ross, P.S., 2013. Partitioning and bioaccumulation of PCBs and PBDEs in marine  
1080 plankton from the Strait of Georgia, British Columbia, Canada. *Progress in Oceanography*,  
1081 115, 65–75. doi: 10.1016/j.pocean.2013.05.023

1082 Galbán-Malagón, C., Berrojalbiz, N., Ojeda, M.J., Dachs, J., 2012. The oceanic biological  
1083 pump modulates the atmospheric transport of persistent organic pollutants to the Arctic.  
1084 *Nature Communications*, 3, 862. doi: 10.1038/ncomms1858

1085 Gasparini, G.P., Zodiatis, G., Astraldi, M., Galli, C., Sparnocchia, S., 1999. Winter  
1086 Intermediate Water lenses in the Ligurian Sea. *Journal of Marine Systems*, 20, 319–332.  
1087 doi: 10.1016/s0924-7963(98)00089-x

1088 Gonzalez, L., Briottet, X., 2017. North Africa and Saudi Arabia day/night sandstorm survey  
1089 (NASCube). *Remote Sensing*, 9, 896. doi: 10.3390/rs9090896

1090 González-Gaya, B., Martínez-Varela, A., Vila-Costa, M., Casal, P., Cerro-Gálvez, E.,  
1091 Berrojalbiz, N., Lundin, D., Vidal, M., Mompean, C., Bode, A., Jiménez, B., Dachs, J.,  
1092 2019. Biodegradation as an important sink of aromatic hydrocarbons in the oceans. *Nature*  
1093 *Geosciences*, 12, 119–125. doi: 10.1038/s41561-018-0285-3

1094 Guieu, C., D’Ortenzio, F., Dulac, F., Taillandier, V., Doglioli, A., Petrenko, A., Barrillon, S.,  
1095 Mallet, M., Nabat, P., Desboeufs, K., 2020. Introduction: Process studies at the air–sea  
1096 interface after atmospheric deposition in the Mediterranean Sea – objectives and strategy  
1097 of the PEACETIME oceanographic campaign (May–June 2017). *Biogeosciences*, 17,  
1098 5563–5585. doi: 10.5194/bg-17-5563-2020, 2020

1099 Guigue, C., Tedetti, M., Ferretto, N., Garcia, N., Méjanelle, L., Goutx, M., 2014. Spatial and  
1100 seasonal variabilities of dissolved hydrocarbons in surface waters from the Northwestern  
1101 Mediterranean Sea: Results from one year intensive sampling. *Science of the Total*  
1102 *Environment*, 466–467, 650–662. doi: 10.1016/j.scitotenv.2013.07.082

1103 Hamza, I., Feki, W., Hamza, A., Bel Hassen, M., 2016. Long term characterization of  
1104 *Trichodesmium erythraeum* blooms in Gabes Gulf (Tunisia). *Continental Shelf Research*,  
1105 124, 95–103. doi: 10.1016/j.csr.2016.05.007

1106 Harmelin-Vivien, M., Cossa, D., Crochet, S., Bănar, D., Letourneur, Y., Mellon-Duval, C.,  
1107 2009. Difference of mercury bioaccumulation in red mullets from the north-western  
1108 Mediterranean and Black seas. *Marine Pollution Bulletin*, 58, 679–685. doi:  
1109 10.1016/j.marpolbul.2009.01.004

1110 Heimbürger, L.E., Cossa, D., Marty, J.C., Migon, C., Averty, B., Dufour, A., Ras, J., 2010.  
1111 Methylmercury distributions in relation to the presence of nano and picophytoplankton in  
1112 an oceanic water column (Ligurian Sea, North-western Mediterranean). *Geochimica*  
1113 *Cosmochimica Acta*, 74, 5549–5559. doi: 10.1016/j.gca.2010.06.036

1114 Heimbürger, L.E., Migon, C., Cossa, D., 2011. Impact of atmospheric deposition of  
1115 anthropogenic and natural trace metals on Northwestern Mediterranean surface waters: A  
1116 box model assessment. *Environmental Pollution*, 159, 1629–1634. doi:  
1117 10.1016/j.envpol.2011.02.046.

1118 Hinrichsen, D., 1990. Our common seas: Coasts in crisis. Earthscan Publications, London, in  
1119 association with United Nations Environment Programme, Nairobi, 184 pp.

1120 Hunt, B.P.V., Carlotti, F., Donoso, K., Pagano, M., D’Ortenzio, F., Taillandier, V., Conan, P.,  
1121 2017. Trophic pathways of phytoplankton size classes through the zooplankton food web  
1122 over the spring transition period in the north-west Mediterranean Sea. *Journal of*  
1123 *Geophysical Research Oceans*, 122, 6309–6324. doi:10.1002/2016JC012658

1124 Jacquet, S., Monnin, C., Herlory, O., Mille, D., Dufour, A., Oursel, B., Heimbürger-Boavida,  
1125 L.E., D’Onofrio, S., Layglon, N., Garnier, C., 2021. Characterization of the submarine  
1126 disposal of a Bayer effluent (Gardanne alumina plant, southern France): I. Size  
1127 distribution, chemical composition and settling rate of particles forming at the outfall.  
1128 *Chemosphere*, 263, 127695. doi: <https://doi.org/10.1016/j.chemosphere.2020.127695>.

1129 Jiskra, M., Heimbürger-Boavida, L.E., Desgranges, M.M., Petrova M.V., Dufour, A.,  
1130 Ferreira-Araujo, B., Masbou, J., Chmeleff, J., Thyssen, M., Point, D., Sonke, J.E., 2021.  
1131 Mercury stable isotopes constrain atmospheric sources to the ocean. *Nature*, 597, 678–682.  
1132 doi: 10.1038/s41586-021-03859-8

1133 Jordi, A., Basterretxea, G., Tovar-Sanchez, A., Alastuey, A., Querol, X., 2012. Copper  
1134 aerosols inhibit phytoplankton growth in the Mediterranean Sea. *Proceedings of the*  
1135 *National Academy of Sciences*, 109, 21246–21249. doi: 10.1073/pnas.1207567110.

1136 Köck-Schulmeyer, M., Ginebreda, A., Petrovic, M., Giulivo, M., Aznar-Alemany, Ò.,  
1137 Eljarrat, E., Valle-Sistac, J., Molins-Delgado, D., Diaz-Cruz, M.S., Monllor-Alcaraz, L.S.,  
1138 Guillem-Argiles, N., Martínez, E., Miren, L.A., Llorca, M., Farré, M., Peña, J.M.,

1139 Mandaric, L., Pérez, S., Majone, B., Bellin, A., Kalogianni, E., Skoulikidis, N.T., Milačić,  
1140 R., Barceló, D., 2021. Priority and emerging organic microcontaminants in three  
1141 Mediterranean river basins: Occurrence, spatial distribution, and identification of river  
1142 basin specific pollutants. *Science of the Total Environment*, 754, 142344. doi:  
1143 10.1016/j.scitotenv.2020.142344

1144 Lascaratos, A., Williams, R.G., Tragou, E., 1993. A mixed-layer study of the formation of  
1145 Levantine Intermediate Water. *Journal of Geophysical Research: Oceans*, 98 (C8), 14739–  
1146 14749.

1147 Leblanc, K., Quéguiner, B., Diaz, F., Cornet, V., Michel-Rodriguez, M., Durrieu de Madron,  
1148 X., Bowler, C., Malviya, S., Thyssen, M., Gregori, G., Rembauville, M., Grosso, O.,  
1149 Poulain, J., de Vargas, C., Pujo-Pay, M., Conan, P., 2018. Nanoplanktonic diatoms are  
1150 globally overlooked but play a role in spring blooms and carbon export. *Nature*  
1151 *Communication*, 9, 953. doi: 10.1038/s41467-018-03376-9

1152 Lee, C.S., Fisher, N.S., 2016. Methylmercury uptake by diverse marine phytoplankton.  
1153 *Limnology and Oceanography*, 61, 1626–1639. doi: 10.1002/lno.10318

1154 Lejeusne, C., Chevaldonné, P., Pergent-Martini, C., Boudouresque, C.F., Pérez, T., 2010.  
1155 Climate change effects on a miniature ocean: the highly diverse, highly impacted  
1156 Mediterranean Sea. *Trends in Ecology and Evolution*, 25, 250–260. doi:  
1157 10.1016/j.tree.2009.10.009

1158 Li, H., Duan, D., Beckingham, B., Yang, Y., Ran, Y., Grathwohl, P., 2020. Impact of trophic  
1159 levels on partitioning and bioaccumulation of polycyclic aromatic hydrocarbons in  
1160 particulate organic matter and plankton. *Marine Pollution Bulletin*, 160, 111527. doi:  
1161 10.1016/j.marpolbul.2020.111527

1162 Li, Z., Chi, J., Wu, Z., Zhang, Y., Liu, Y., Huang, L., Lu, Y., Uddin, M., Zhang, W., Wand,  
1163 X., Lin, Y., Tong, Y., 2021. Characteristics of plankton Hg bioaccumulations based on a

1164 global data set and the implications for aquatic systems with aggravating nutrient  
1165 imbalance. *Frontiers of Environmental Science & Engineering*, 16, 37. doi:  
1166 10.1007/s11783-021-1471-x

1167 Lipiatou, E., Albaigés, J., 1994. Atmospheric deposition of hydrophobic organic chemicals in  
1168 the northwestern Mediterranean Sea: comparison with the Rhone river input. *Marine*  
1169 *Chemistry*, 46, 153–164. doi: 10.1016/0304-4203(94)90052-3

1170 Llamas-Dios, M.I., Vadillo, I., Jimenez-Gavilan, P., Candela, L., Corada-Fernandez, C., 2021.  
1171 Assessment of a wide array of contaminants of emerging concern in a Mediterranean water  
1172 basin (Guadalhorce river, Spain): Motivations for an improvement of water management  
1173 and pollutants surveillance. *Science of the Total Environment*, 788, 147822. doi:  
1174 0.1016/j.scitotenv.2021.147822

1175 Marañón, E., Wambeke, F., Uitz, J., Boss, E., Dimier, C., Dinasquet, J., Engel, A., Haëntjens,  
1176 N., Pérez-Lorenzo, M., Taillandier, V., Zäncker, B., 2021. Deep maxima of phytoplankton  
1177 biomass, primary production and bacterial production in the Mediterranean Sea.  
1178 *Biogeosciences*, 18, 1749–1767. doi: 10.5194/bg-18-1749-2021

1179 Margirier, F., Testor, P., Heslop, E., Mallil, K., Bosse, A., Houpert, L., Mortier, L., Bouin,  
1180 M.-N., Coppola, L., D’Ortenzio, F., Durrieu de Madron, X., Moure, B., Prieur, L.,  
1181 Raimbault, P., Taillandier, V., 2020. Abrupt warming and salinification of intermediate  
1182 waters interplays with decline of deep convection in the Northwestern Mediterranean Sea.  
1183 *Scientific Reports*, 10, 20923. doi: 10.1038/s41598-020-77859-5

1184 Martin, J.H., Knauer, G.A., 1973. The elemental composition of plankton. *Geochimica*  
1185 *Cosmochimica Acta*, 37, 1639–1653. doi: 10.1016/0016-7037(73)90154-3

1186 Mayot, N., D’Ortenzio, F., Uitz, J., Gentili, B., Ras, J., Vellucci, V., Golbol, M., Antoine, D.,  
1187 Claustre, H., 2017. Influence of the Phytoplankton Community Structure on the Spring and

1188 Annual Primary Production in the Northwestern Mediterranean Sea, *Journal of*  
1189 *Geophysical Research Oceans*, 122, 9918–9936. doi:10.1002/2016JC012668

1190 Millot, C., 1999. Circulation in the Western Mediterranean Sea. *Journal of Marine Systems*,  
1191 20, 423–442. doi: 10.1016/S0924-7963(98)00078-5

1192 Millot, C., Taupier-Letage, I., 2005. Circulation in the Mediterranean Sea. *The Handbook of*  
1193 *Environmental Chemistry*, vol. K 29–66. doi: 10.1007/b107143

1194 Morales, L., Dachs, J., Fernández-Pinos, M.C., Berrojalbiz, N., Mompean, C., González-  
1195 Gaya, B., Jiménez, B., Bode, A., Abalos, M., Abad, E., 2015. Oceanic sink and  
1196 biogeochemical controls on the accumulation of polychlorinated dibenzo-pdioxins,  
1197 dibenzofurans, and biphenyls in plankton. *Environmental Science and Technology*, 49,  
1198 13853–13861. doi: 10.1021/acs.est.5b01360

1199 Nizzetto, L., Gioia, R., Li, J., Borga, K., Pomati, F., Bettinetti, R., Dachs, J., Jones, K.C.,  
1200 2012. Biological pump control of the fate and distribution of hydrophobic organic  
1201 pollutants in water and plankton. *Environmental Science and Technology*, 46, 3204–3211.  
1202 doi: 10.1021/es204176q

1203 Oursel, B., Garnier, C., Durrieu, G., Mounier, S., Omanović, D., Lucas, Y., 2013. Dynamics  
1204 and fates of trace metals chronically input in a Mediterranean coastal zone impacted by a  
1205 large urban area. *Marine Pollution Bulletin*, 69, 137–149. doi:  
1206 10.1016/j.marpolbul.2013.01.023

1207 Radakovitch, O., Roussiez, V., Ollivier, P., Ludwig, W., Grenz, C., Probst, J.L., 2008.  
1208 Particulate heavy metals input from rivers and associated sedimentary deposits on the Gulf  
1209 of Lion continental shelf. *Estuarine, Coastal and Shelf Science*, 77, 285–295. doi:  
1210 10.1016/j.ecss.2007.09.028

1211 Ramírez-Romero, E., Molinero, J.C., Sommer, U., Salhi, N., Kefi- Daly Yahia, O., Daly  
1212 Yahia, M.N., 2020. Phytoplankton size changes and diversity loss in the southwestern



1213 Mediterranean Sea in relation to long-term hydrographic variability. *Estuarine, Coastal and*  
1214 *Shelf Science*, 235, 106574. doi: 10.1016/j.ecss.2019.106574

1215 Reygondeau, G., Guieu, C., Benedetti, F., Irisson, J.O., Ayata, S.D., Gasparini, S., Koubbi, P.,  
1216 2017. Biogeochemical regions of the Mediterranean Sea: an objective multidimensional  
1217 and multivariate environmental approach. *Progress in Oceanography*, 151, 138–148. doi:  
1218 10.1016/j.pocean.2016.11.001

1219 Reygondeau, G., Irisson, J.-O., Ayata, S., Gasparini, S., Benedetti, F., Albouy, C., Hattab, T.,  
1220 Guieu, C., Koubbi, P., 2014. Definition of the Mediterranean Eco-Regions and Maps of  
1221 Potential Pressures in These Eco-Regions. Technical Report. Deliverable Nr. 1.6. FP7-  
1222 PERSEUS project.

1223 Salat, J., Font, J., 1987. Water mass structure near and off shore the Catalan coast during the  
1224 winters of 1982 and 1983. *Annales Geophysicae*, 1B, 49–54.

1225 Salgado-Hernanz, P.M., Racault, M.-F., Font-Muñoz, J.S., Basterretxea, G., 2019. Trends in  
1226 phytoplankton phenology in the Mediterranean Sea based on ocean-colour remote sensing.  
1227 *Remote Sensing of Environment*, 221, 50–64. doi: 10.1016/j.rse.2018.10.036

1228 Salhi, N., Zmerli Triki, H., Molinero, J.C., Laabir, M., Sehli, E., Bellaaj-Zouari, A., Daly  
1229 Yahia, N., Kefi-Daly Yahia, O., 2018. Seasonal variability of picophytoplankton under  
1230 contrasting environments in northern Tunisian coasts, southwestern Mediterranean Sea.  
1231 *Marine Pollution Bulletin*, 129, 866–874. doi: 10.1016/j.marpolbul.2017.10.029

1232 Schlitzer, R., 2014. Ocean Data View. Available online at: <http://odv.awi.de>

1233 Ser-Giacomi, E., Jordá-Sánchez, G., Sotto-Navarro, J., Thomsen, S., Mignot, J., Sevault, F.,  
1234 Rossi, V., 2020. Impact of climate change on surface stirring and transport in the  
1235 Mediterranean Sea. *Geophysical Research Letters*, 47, e2020GL089941. doi:  
1236 10.1029/2020GL089941

1237 Sicre, M.-A., Fernandes, M.B., Pont, D., 2008. Poly-aromatic hydrocarbon (PAH) inputs from  
1238 the Rhône River to the Mediterranean Sea in relation with the hydrological cycle: Impact  
1239 of floods. *Marine Pollution Bulletin*, 56, 1935–1942. doi: 10.1016/j.marpolbul.2008.07.015  
1240 Siokou-Frangou, I., Christaki, U., Mazzocchi, M.G., Montresor, M., Ribera D'Alcala, M.,  
1241 Vaque, D., Zingone, A., 2010. Plankton in the open mediterranean Sea: A review.  
1242 *Biogeosciences*, 7, 1543–1586. doi: 10.5194/bg-7-1543-2010  
1243 Strady, E., Harmelin-Vivien, M., Chiffoleau, J.F., Veron, A., Tronczynski, J., Radakovitch,  
1244 O., 2015. <sup>210</sup>Po and <sup>210</sup>Pb trophic transfer within the phytoplankton–zooplankton–  
1245 anchovy/sardine food web: a case study from the Gulf of Lion (NW Mediterranean Sea).  
1246 *Journal of Environmental Radioactivity*, 143, 141–151. doi: 10.1016/j.jenvrad.2015.02.019  
1247 Swackhamer, D.L., Skoglund, R.S., 1993. Bioaccumulation of PCBs by algae: kinetics versus  
1248 equilibrium. *Environmental Toxicology and Chemistry*, 12, 831–838. doi:  
1249 10.1002/etc.5620120506  
1250 Tang, J., Wang, S., Tai, Y., Tam, N.F., Su, L., Shi, Y., Luo, B., Tao, R., Yang, Y., Zhang, X.,  
1251 2020. Evaluation of factors influencing annual occurrence, bioaccumulation, and  
1252 biomagnification of antibiotics in planktonic food webs of a large subtropical river in  
1253 South China. *Water Research*, 170, 115302. doi: 10.1016/j.watres.2019.115302  
1254 Tao, Y., Xue, B., Lei, G., Liu, F., Wang, Z., 2017a. Effects of climate change on  
1255 bioaccumulation and biomagnification of polycyclic aromatic hydrocarbons in the  
1256 planktonic food web of a subtropical shallow eutrophic lake in China. *Environmental*  
1257 *Pollution*, 223, 624–634. doi: 10.1016/j.envpol.2017.01.068  
1258 Tao, Y., Yu, J., Liu, X., Xue, B., Wang, S., 2018. Factors affecting annual occurrence,  
1259 bioaccumulation, and biomagnification of polycyclic aromatic hydrocarbons in plankton  
1260 food webs of subtropical eutrophic lakes. *Water Research*, 132, 1–11. doi:  
1261 10.1016/j.watres.2017.12.053

1262 Tao, Y., Yu, J., Xue, B., Yao, S., Wang, S., 2017b. Precipitation and temperature drive  
1263 seasonal variation in bioaccumulation of polycyclic aromatic hydrocarbons in the  
1264 planktonic food webs of a subtropical shallow eutrophic lake in China. *Science of the Total*  
1265 *Environment*, 583, 447–457. doi: 10.1016/j.scitotenv.2017.01.100

1266 Tedetti, M., Guigue, C., Goutx, M., 2010. Utilization of a submersible UV fluorometer for  
1267 monitoring anthropogenic inputs in the Mediterranean coastal waters. *Marine Pollution*  
1268 *Bulletin*, 60, 350–362. doi: 10.1016/j.marpolbul.2009.10.018

1269 Tedetti, M., Tronczynski, J., 2019. HIPPOCAMPE cruise, RV Antea.  
1270 <https://doi.org/10.17600/18000900>

1271 Tesán-Onrubia, J.A., Tedetti, M., Carlotti, F., Tenaille, M., Guilloux, L., Pagano, M.,  
1272 Lebreton, B., Guillou, G., Fierro-González, P., Guigue, C., Chifflet, S., Garcia, T.,  
1273 Boudriga, I., Belhassen, M., Bellaaj-Zouari, M., Bănar, D., 2023. Spatial variations of  
1274 stable isotope compositions and biochemical content of size-fractionated plankton in the  
1275 Mediterranean Sea (MERITE-HIPPOCAMPE campaign). In revision to this special issue.

1276 The MerMex Group, 2011. Marine ecosystems' responses to climatic and anthropogenic  
1277 forcings in the Mediterranean. *Progress in Oceanography*, 91, 97–166. doi:  
1278 10.1016/j.pocean.2011.02.003

1279 Thieuleux, F., Moulin, C., Bréon, F.M., Maignan, F., Poitou, J., Tanré, D., 2005. Remote  
1280 sensing of aerosols over the oceans using MSG/SEVIRI imagery. *Annals of Geophysics*,  
1281 23, 3561–3568. doi: 10.5194/angeo-23-3561-2005

1282 Thomas, D.M., Lee, C.-S., Fisher, N.S., 2018. Bioaccumulation and trophic transfer of <sup>137</sup>Cs  
1283 in marine and freshwater plankton. *Chemosphere*, 209, 599–607. doi:  
1284 10.1016/j.chemosphere.2018.06.124

1285 Tiano, M., Tronczyński, J., Harmelin-Vivien, M., Tixier, C., Carlotti, F., 2014. PCB  
1286 concentrations in plankton size classes, a temporal study in Marseille Bay, Western

1287 Mediterranean Sea. *Marine Pollution Bulletin*, 89, 331–339. doi:  
1288 10.1016/j.marpolbul.2014.09.040

1289 Tornero, V., Hanke, G., 2016. Chemical contaminants entering the marine environment from  
1290 sea-based sources: A review with a focus on European seas. *Marine Pollution Bulletin*,  
1291 112, 17–38. doi: <https://doi.org/10.1016/j.marpolbul.2016.06.091>

1292 Uitz, J., Claustre, H., Morel, A., Hooker, S.B., 2006. Vertical distribution of phytoplankton  
1293 communities in open ocean: An assessment based on surface chlorophyll. *Journal of*  
1294 *Geophysical Research Oceans*, 111, C08005. doi:10.1029/2005JC003207

1295 UNEP/MAP, 2012. *State of the Mediterranean Marine and Coastal Environment*,  
1296 UNEP/MAP – Barcelona Convention, Athens.

1297 Vargaz-Yanez, M., Mallard, E.R.M., Zunino, P., Garcia-Martinez, M., Moya, F., 2012. The  
1298 effect of interpolation methods in temperature and salinity trends in the western  
1299 Mediterranean. *Mediterranean Marine Science*, 13, 118–125. doi: 10.12681/mms.28

1300 Volpe, G., Colella, S., Brando, V.E., Forneris, V., La Padula, F., Di Cicco, A., Sammartino,  
1301 M., Bracaglia, M., Artuso, F., Santoleri, R., 2019. Mediterranean ocean colour Level 3  
1302 operational multi-sensor processing. *Ocean Science*, 15, 127–146. doi: 10.5194/os-15-127-  
1303 2019

1304 Zouch, H., Cabrol, L., Chifflet, S., Tedetti, M., Karray, F., Zaghden, H., Sayadi, S.,  
1305 Quéméneur, M., 2018. Effect of acidic industrial effluent release on microbial diversity  
1306 and trace metal dynamics during resuspension of coastal sediment. *Frontiers in*  
1307 *Microbiology*, 9, 3103, doi: 10.3389/fmicb. 2018.03103

1308

1309

1310

1311

1312 **Figure captions**

1313

1314 **Figure 1.** Conceptual scheme and questions addressed by the MERITE-HIPPOCAMPE  
1315 cruise to identify the role of Mediterranean plankton as biological pump of contaminants. It  
1316 considers the accumulation and transfer of metallic/metalloid/organometallic and organic  
1317 contaminants at the atmosphere-water-plankton interfaces and through the planktonic food  
1318 webs, i.e., phyto-, zoo- and bacterio-plankton, with the deep chlorophyll maximum (DCM) as  
1319 privileged study zone.

1320

1321 **Figure 2.** a) Location of the ten stations (black circles) investigated during the MERITE-  
1322 HIPPOCAMPE cruise (13 April–14 May 2019) along a North-South transect in the  
1323 Mediterranean Sea on board the R/V *Antea*. The main characteristics of these stations are  
1324 provided in [Table 1](#). In addition, two other stations (T2 and T4, brown circles) were sampled  
1325 in the Tunisian waters during leg 2 (2–3 May 2019) on board the R/V *Hannibal* for trawling  
1326 of small pelagic fishes (see [Table 2](#) for more details). Two ground stations, located in the  
1327 northern part (Marseille, France) and southern part (Sfax, Tunisia) of the Mediterranean  
1328 basin, were set up for the collection of atmospheric deposition samples from March 2019 to  
1329 June 2020 (i.e., before, during and after the cruise). b) Cruise track with the position of the ten  
1330 stations studied on board the R/V *Antea*. During leg 1 (13–28 April; from La Seyne-sur-Mer  
1331 to Tunis), five stations were sampled: St2, St4, St3, S10 and St11 (in this chronological  
1332 order), while the five other stations were sampled during leg 2 (30 April–14 May; from Tunis  
1333 to Gulf of Gabès, and then return to La Seyne-sur-Mer): St15, St17, St19, St9 and St1 (in this  
1334 chronological order).

1335

1336 **Figure 3.** Summary of our approach with 1) the collection of large amounts of plankton,  
1337 suspended particles, and water in the deep chlorophyll maximum (DCM) and  
1338 surface/subsurface waters (0–5 m depth) with various collecting instruments, 2) the separation  
1339 of these materials into diverse size fractions by sieving or filtration, and the sharing of the  
1340 obtained size fractions for numerous biological and chemical analyses. Adapted from [Alcaraz](#)  
1341 [and Calbet \(2003\)](#).

1342

1343 **Figure 4.** Saharan dust event of April. Here is presented for 22 April 2019 which is the day  
1344 where the dust plume was the most intense: a) Daily Aerosol Optical Depth (AOD, unitless)  
1345 product from MSG-SEVIRI, b) MODIS image from NASA worldview, and BSC-DREAM-  
1346 Dust forecast of c) dry and d) wet deposition (in  $\text{mg m}^{-2}$ ).

1347

1348 **Figure 5.** Saharan dust event of May. Here is presented for 3 May 2019 which is the day  
1349 where the dust was located over ship's position: a) Daily Aerosol Optical Depth (AOD,  
1350 unitless) product from MSG-SEVIRI, b) MODIS image from NASA worldview, and BSC-  
1351 DREAM-Dust forecast of c) dry and d) wet deposition (in  $\text{mg m}^{-2}$ ).

1352

1353 **Figure 6.** Distribution of subsurface **a)** temperature ( $^{\circ}\text{C}$ ) and **b)** salinity along the North-  
1354 South Mediterranean transect recorded continuously from the flow-through pumped seawater  
1355 at 2-m depth. Ocean Data View (ODV) software version 4.6.5. Schlitzer, R.,  
1356 <http://odv.awi.de>. 2014.

1357

1358 **Figure 7.** Vertical profiles of temperature ( $^{\circ}\text{C}$ ), salinity, TChla concentration ( $\mu\text{g L}^{-1}$ ) and  
1359 dissolved  $\text{O}_2$  concentration ( $\mu\text{mole kg}^{-1}$ ) issued from the main carousel CTD deployments  
1360 (Seabird SBE 911*plus*) at stations St1–St9. The dotted lines represent the depth of sampling in

1361 the deep chlorophyll maximum (DCM) for Niskin/Go-Flo bottles. In box, the depth of the  
1362 station. One or two profiles are displayed for each station. For each profile, only data acquired  
1363 during the upcast are presented.

1364  
1365 **Figure 8.** Vertical profiles of temperature ( $^{\circ}\text{C}$ ), salinity, TChla concentration ( $\mu\text{g L}^{-1}$ ) and  
1366 dissolved  $\text{O}_2$  concentration ( $\mu\text{mole kg}^{-1}$ ) issued from the main carousel CTD deployments  
1367 (Seabird SBE 911*plus*) at stations St10–St19. The dotted lines represent the depth of sampling  
1368 in the deep chlorophyll maximum (DCM) for Niskin/Go-Flo bottles. In box, the depth of the  
1369 station. One or two profiles are displayed for each station. For each profile, only data acquired  
1370 during the upcast are presented.

1371  
1372 **Figure 9.** Temperature-salinity diagram and identification of the main waters masses  
1373 encountered during the MERITE-HIPPOCAMPE cruise (RAW: resident Atlantic Water;  
1374 NAW: new Atlantic Water; LIW: Levantine Intermediate Water; WIW: Western  
1375 Mediterranean Intermediate Water; GG: Gulf of Gabès water). The colour code refers to a)  
1376 depth (in m) and b) stations (St1–St19). Twenty-one carousel CTD casts were used for this  
1377 plot. Ocean Data View (ODV) software version 4.6.5. Schlitzer, R., <http://odv.awi.de>. 2014.

1378  
1379 **Figure 10.** Composite image of average surface chlorophyll *a* (Chla) concentration (in  $\mu\text{g L}^{-1}$ )  
1380 over the period (13 April–14 May 2019) and area of the MERITE-HIPPOCAMPE cruise  
1381 from Multi Satellite products (MODIS-AQUA, NOAA20-VIIRS, NPP-VIIRS and  
1382 Sentinel3A-OLCI) (L4 product level, 1-km resolution; [Volpe et al., 2019](#)). This composite  
1383 image corresponds to the average of the 32 daily images (from 13 April to 14 May 2019) for  
1384 which Chla concentration was averaged during the 8 h of measurements in the area. Product

1385 name: OCEANCOLOUR\_MED\_CHL\_L4\_REP\_OBSERVATIONS\_009\_078. Obtained  
1386 from EU Copernicus Marine Service Information (CMEMS; <https://marine.copernicus.eu/>).  
1387

1388 **Figure 11.** Distribution of various biogeochemical parameters recorded at the deep  
1389 chlorophyll maximum (DCM) across the ten stations, from the most coastal stations in the  
1390 North (St1, St4) to the southernmost stations (St17, St19): a) depth of the DCM (in m),  
1391 concentrations in b) total chlorophyll *a* (TChl*a*, in  $\mu\text{g L}^{-1}$ ), c) particulate organic carbon  
1392 (POC, in  $\mu\text{g L}^{-1}$ ), d) silicates [ $\text{Si}(\text{OH})_4$ , in  $\mu\text{M}$ ], e) nitrates ( $\text{NO}_3^-$ , in  $\mu\text{M}$ ), f) phosphates ( $\text{PO}_4^{3-}$   
1393 , in  $\mu\text{M}$ ), g) dissolved organic carbon (DOC, in  $\mu\text{M}$ ), and h) absorption of chromophoric  
1394 dissolved organic matter at 254 nm ( $a_{\text{CDOM}}$ , in  $\text{m}^{-1}$ ). Nutrients, DOC and  $a_{\text{CDOM}}$  were  
1395 measured on the fraction  $< 0.7 \mu\text{m}$ , while TChl*a* and POC were measured on the fraction  $>$   
1396  $0.7 \mu\text{m}$  from samples collected with Niskin X bottles.

1397  
1398 **Figure 12.** Principal component analysis (PCA), based on the Pearson's correlation matrix,  
1399 applied on the main biogeochemical parameters recorded at each stations (St1–19) in the deep  
1400 chlorophyll maximum (DCM): concentrations in silicates [ $\text{Si}(\text{OH})_4$ , in  $\mu\text{M}$ ], nitrates ( $\text{NO}_3^-$ , in  
1401  $\mu\text{M}$ ), phosphates ( $\text{PO}_4^{3-}$ , in  $\mu\text{M}$ ), total chlorophyll *a* (TChl*a*, in  $\mu\text{g L}^{-1}$ ), particulate organic  
1402 carbon (POC, in  $\mu\text{g L}^{-1}$ ), dissolved organic carbon (DOC, in  $\mu\text{M}$ ) and absorption of  
1403 chromophoric dissolved organic matter at 254 nm ( $a_{\text{CDOM}}$ , in  $\text{m}^{-1}$ ). Projection of variables (i.e.,  
1404 main biogeochemical parameters, in red) and distribution of samples (i.e., stations, in blue) on  
1405 the first factorial plane (PC1 *versus* PC2). Four groups of samples (stations) are highlighted  
1406 from this PCA and confirmed by a hierarchical ascendant classification (dissimilarity  
1407 measurement between clusters based on Ward's method): 1) St2, St3, St4, St10, 2) St1, St11,  
1408 St15, St17, 3) St9, and 4) St19.

1409



1410 **Figure 13.** Overview of the types of articles that are a part of this special issue in the frame of  
1411 the MERITE-HIPPOCAMPE cruise.

1412 **Table 1.** Main characteristics of the ten stations investigated in spring during the MERITE-HIPPOCAMPE cruise (13 April–14 May 2019) on  
 1413 board the R/V *Antea* along a North-South transect in the Mediterranean Sea. The stations are presented in chronological order in leg 1 then leg 2.  
 1414

Leg	Station	Latitude (N)	Longitude (E)	Location	Features	Area	Depth (m)	Start of operations (dd/mm in 2019)	End of operations (dd/mm in 2019)
1	St2	42° 56.020'	5° 58.041'	Offshore Toulon	Limit of the continental shelf; Boundary of the Ligurian consensus region <sup>d</sup> ; Intermittently bloom area or bloom area (cluster #4 or #5) <sup>e</sup>	French	1770	14/04	16/04
	St4	43° 14.500'	5° 17.500'	Bay of Marseille (SOLEMIO <sup>a</sup> station)	Urbanised bay; Intermittently bloom area or bloom area (cluster #4 or #5) <sup>e</sup>	French	58	16/04	18/04
	St3	43° 08.150'	5° 15.280'	Offshore Marseille (JULIO <sup>b</sup> station)	Southeast entrance to the Gulf of Lion; Intrusions of the Ligurian-Provençal current; Intermittently bloom area or bloom area (cluster #4 or #5) <sup>e</sup>	French	95	18/04	20/04
	St10	40° 18.632'	7° 14.753'	Offshore (station 2 of PEACETIME cruise <sup>c</sup> )	Slightly north of the North Balearic Front; Intermittently bloom area (cluster #4) <sup>e</sup>	Italian	2791	22/04	24/04
	St11	39° 07.998'	7° 41.010'	Offshore (station 3 of PEACETIME cruise <sup>c</sup> )	South of the North Balearic Front; Algerian consensus region <sup>d</sup> ; Presence of mesoscale eddies; No bloom area (cluster #3) <sup>e</sup>	Italian	1378	25/04	26/04

2	St15	36° 12.883'	11° 07.641'	Gulf of Hammamet	Close to the Sicily Channel; Possible entrance of Atlantic Tunisian Current branch; No bloom area (cluster #3) <sup>e</sup> ; High density of small pelagic fishes	Tunisian	100	29/04	30/04
	St17	34° 30.113'	11° 43.573'	North of Gulf of Gabès	Gabès consensus region <sup>d</sup> boundary; Shallow area, influence of tides and Atlantic Tunisian Current; Coastal bloom area (cluster #6) <sup>e</sup> ; High density of small pelagic fishes	Tunisian	50	01/05	02/05
	St19	33° 51.659'	11° 18.509'	South of Gulf of Gabès	Gabès consensus region <sup>d</sup> ; Shallow area, influence of tides and Atlantic Tunisian Current; Coastal bloom area (cluster #6) <sup>e</sup> ; High density of small pelagic fishes	Tunisian	50	02/05	05/05
	St9	41° 53.508'	6° 19.998'	Offshore (station 1 of PEACETIME cruise <sup>e</sup> )	North of the North Balearic Front; Boundary of the Ligurian consensus region <sup>d</sup> ; Winter convection area; Bloom area (cluster #5) <sup>e</sup>	French	2575	08/05	09/05
	St1	43° 03.819'	5° 59.080'	Bay of Toulon	Nearly closed urbanised bay; Intermittently bloom area or bloom area (cluster #4 or #5) <sup>e</sup>	French	91	10/05	11/05

1415 <sup>a</sup> The SOLEMIO station (*Site d'Observation Littoral pour l'Environnement du MIO*) is part of the French national network of coastal observation SOMLIT  
1416 (*Service d'Observation en Milieu LITtoral* – <http://somlit.epoc.u-bordeaux1.fr/fr/>).

1417 <sup>b</sup> The JULIO station (*JUdicious Location for Intrusions Observations*) is dedicated to the study of the intrusions of the Ligurian-Provençal current.

1418 <sup>c</sup> The PEACETIME cruise (*ProcEss studies at the Air-sEa Interface after dust deposition in the MEditerranean sea*) took place in May-June 2017

1419 (<http://peacetime-project.org/>; Guieu et al., 2020).

1420 <sup>d</sup> Consensus regions of the Mediterranean Sea as defined by Ayata et al. (2018).

1421 <sup>e</sup> Bloom/cluster areas as defined by D'Ortenzio and d'Alcalà (2009) from SeaWiFS satellite surface TChla concentration observations.

1422

1423

1424 **Table 2.** Main characteristics of the two stations investigated during the MERITE-  
1425 HIPPOCAMPE cruise in May 2019 on board the R/V *Hannibal* in the Tunisian waters for  
1426 trawling of small pelagic fishes.

1427

<b>Station</b>	<b>Latitude (N)</b>	<b>Longitude (E)</b>	<b>Location</b>	<b>Depth (m)</b>	<b>Date (dd/mm in 2019)</b>	<b>Trawling duration</b>
T2	34° 11.892'	10° 58.152'	Gulf of Gabès	45	02/05	0h40
T4	36° 59.142'	10° 19.734'	Gulf of Tunis	37	03/05	1h30

1428

1429

1430

1431

1432

**Table 3.** Information about wet (rain) atmospheric deposition samples collected on board the R/V *Antea* during the MERITE-HIPPOCAMPE cruise.

<b>Sample</b>	<b>Station</b>	<b>Start date of sampling</b>	<b>Start time of sampling (UT)</b>	<b>End date of sampling (dd/mm in 2019)</b>	<b>End time of sampling (UT)</b>	<b>Type of deposition</b>
Rain 1	St10	22/04/19	19h15	23/04	9h45	Rain
Rain 2	St10	24/04/19	7h30	24/04	12h30	Rain
Rain 3	St11	26/04/19	3h15	26/04	12h00	Rain
Rain 4	St19	03/05/19	5h45	03/05	14h00	Rain
Rain 5	Transit from off Djerba to off Zarzis	03/05/19	16h45	04/05	9h00	Dry deposition + rain
Rain 6	St1	11/05/19	3h00	11/05	6h15	Rain

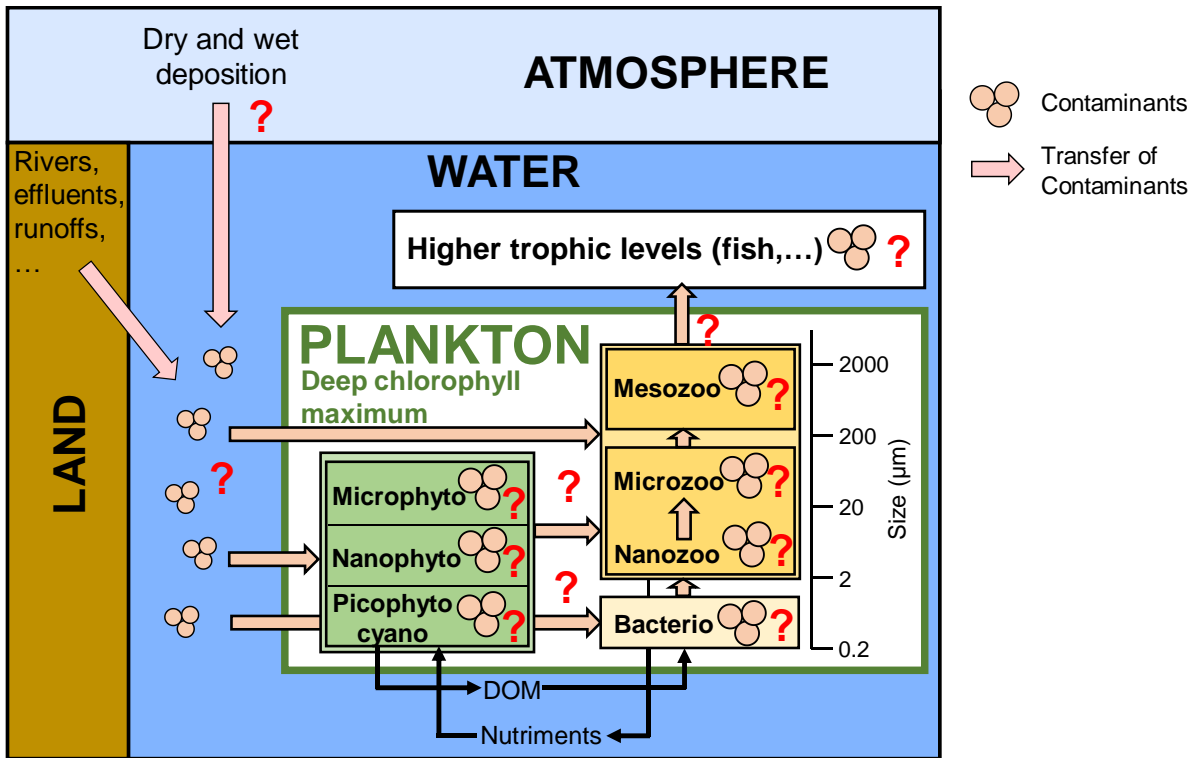


Figure 1

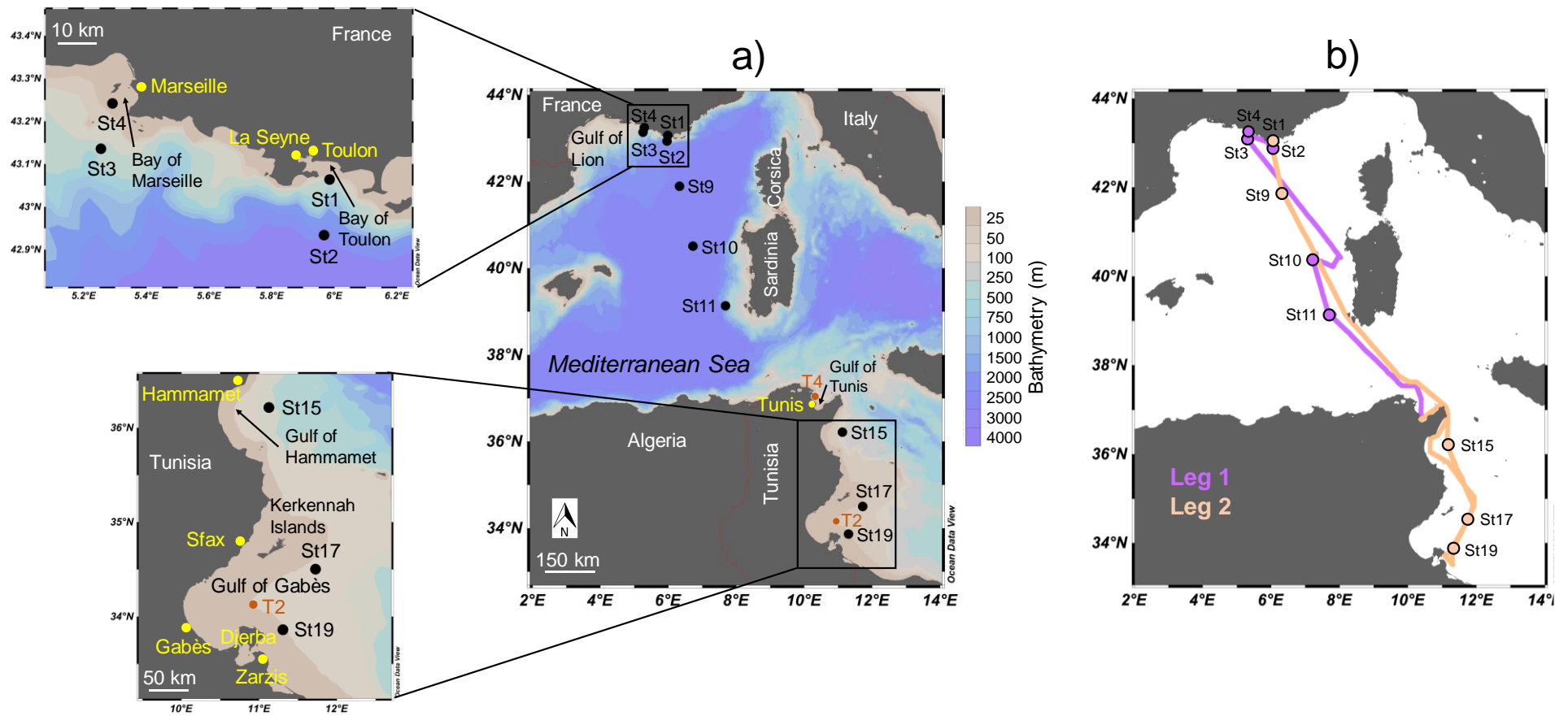


Figure 2

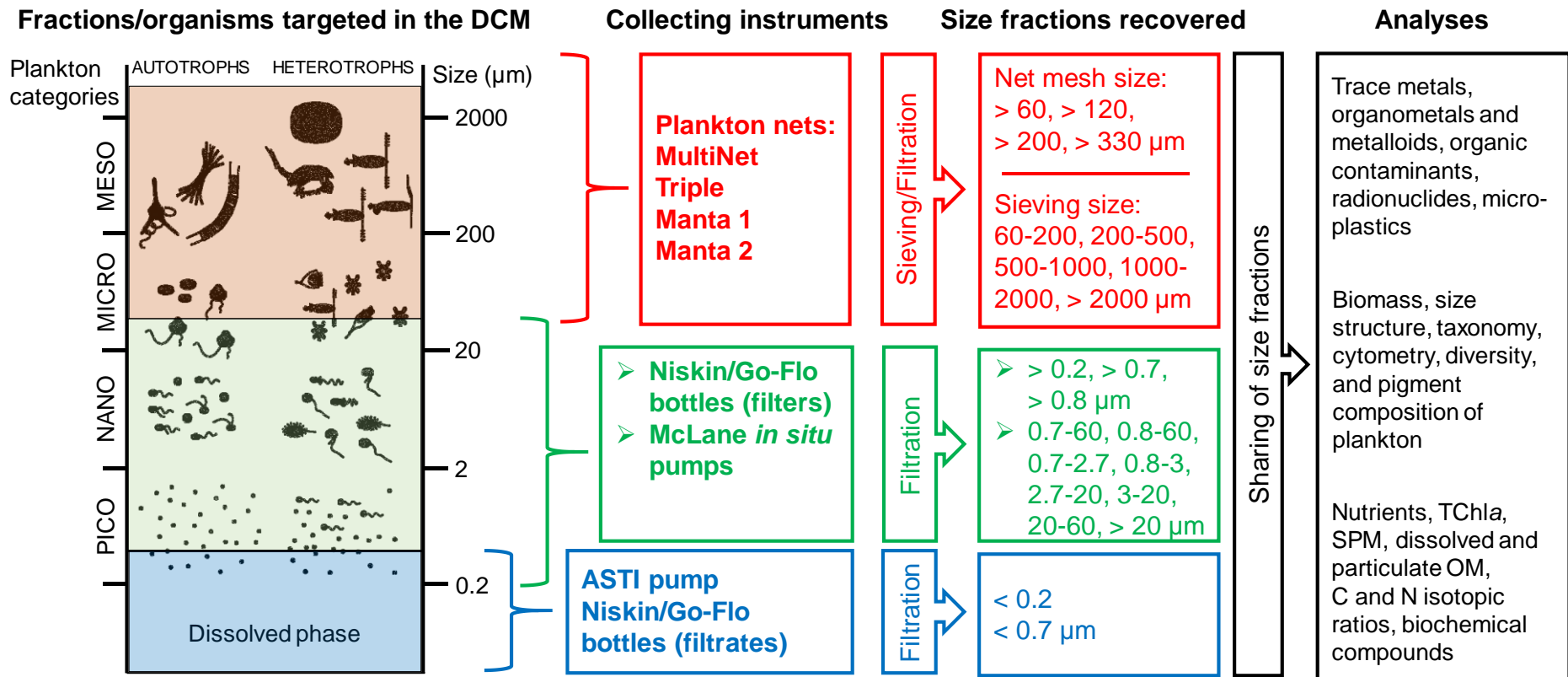


Figure 3



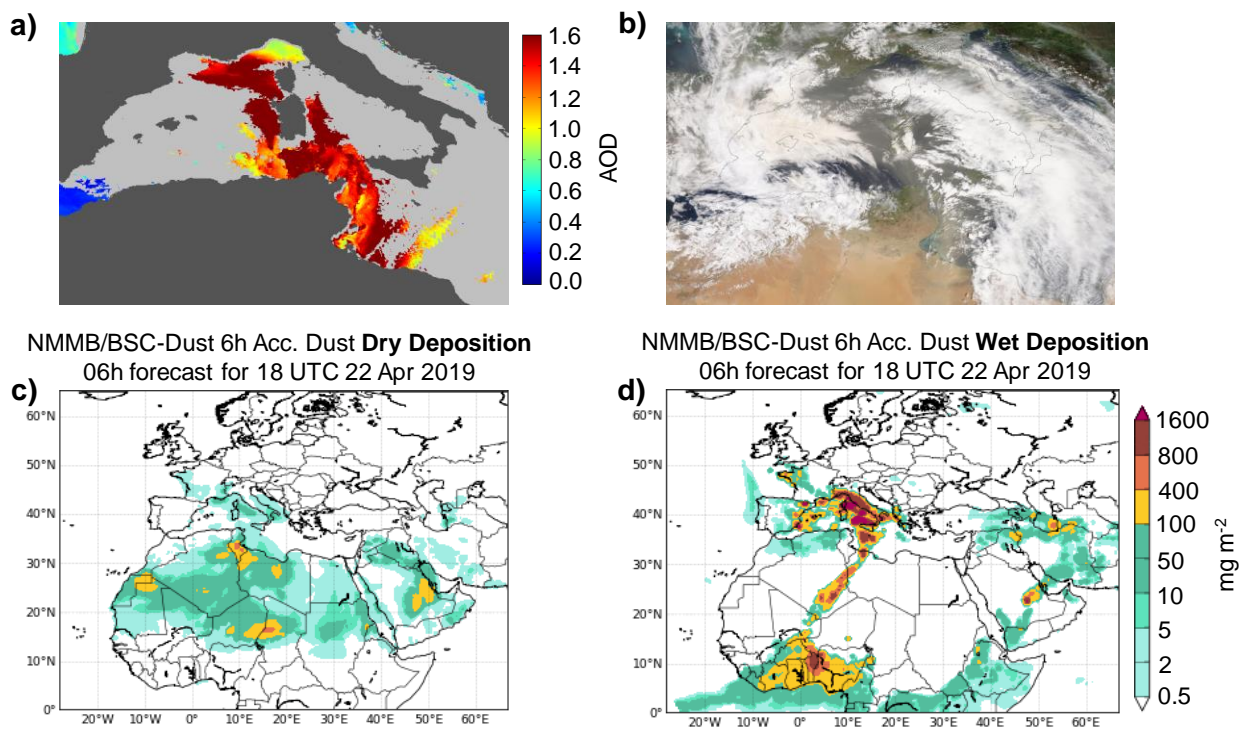
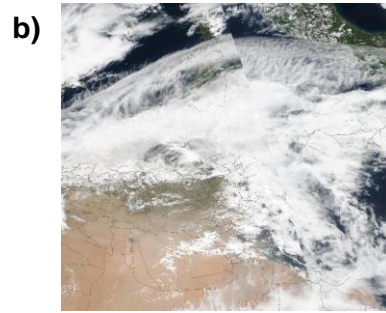
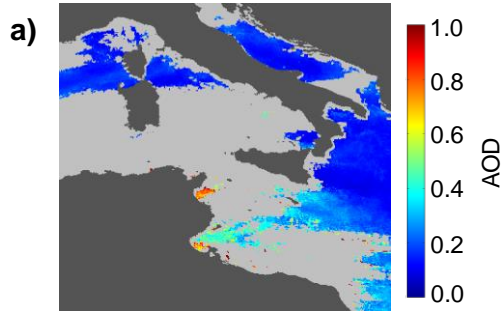
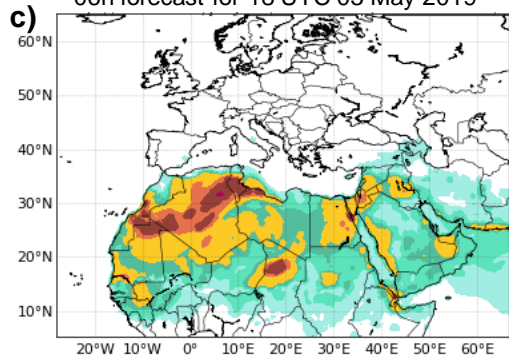


Figure 4



NMMB/BSC-Dust 6h Acc. Dust **Dry Deposition**  
06h forecast for 18 UTC 03 May 2019



NMMB/BSC-Dust 6h Acc. Dust **Wet Deposition**  
06h forecast for 18 UTC 03 May 2019

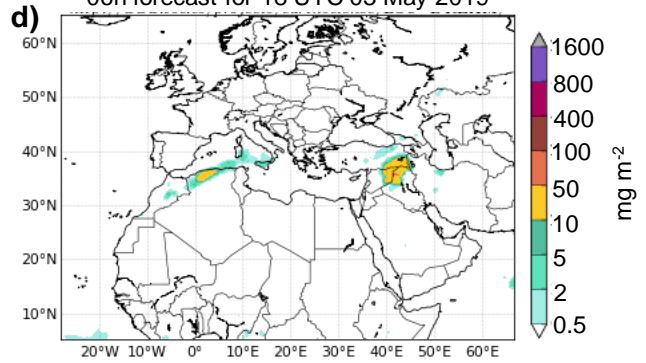


Figure 5

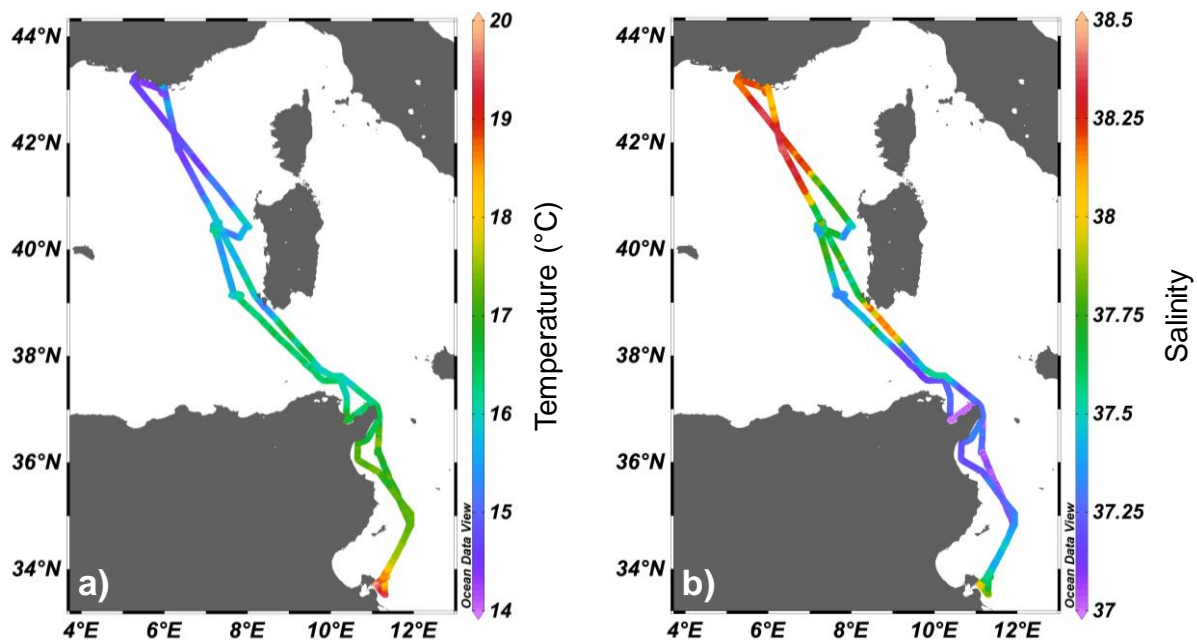


Figure 6

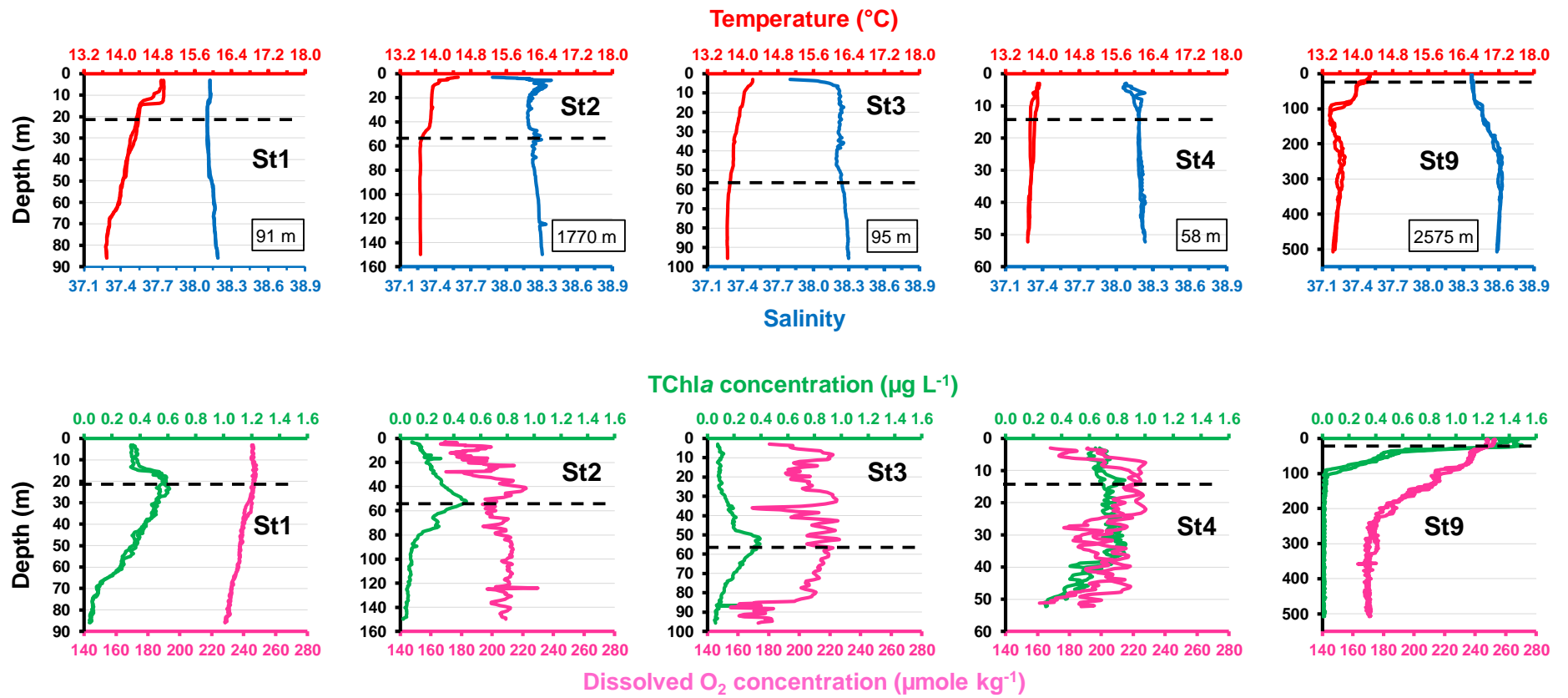


Figure 7

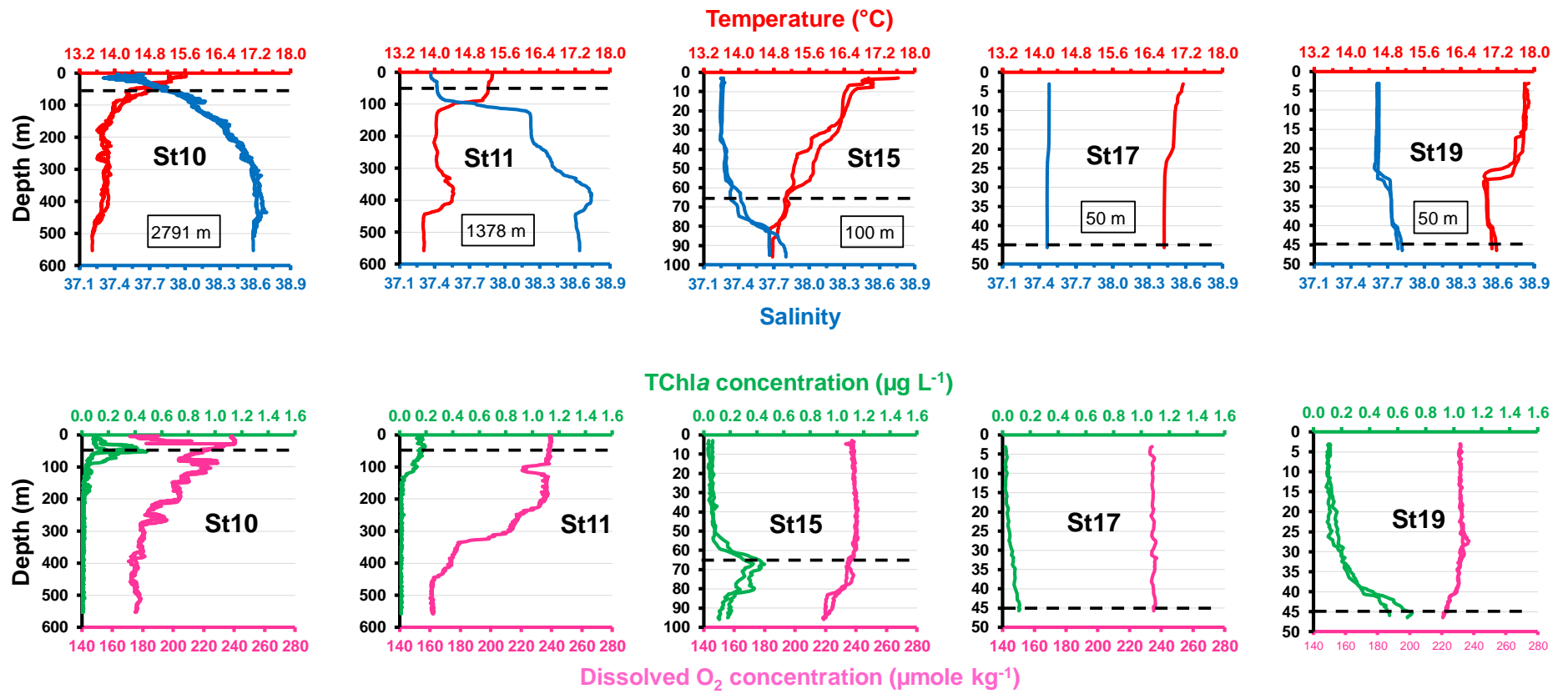


Figure 8

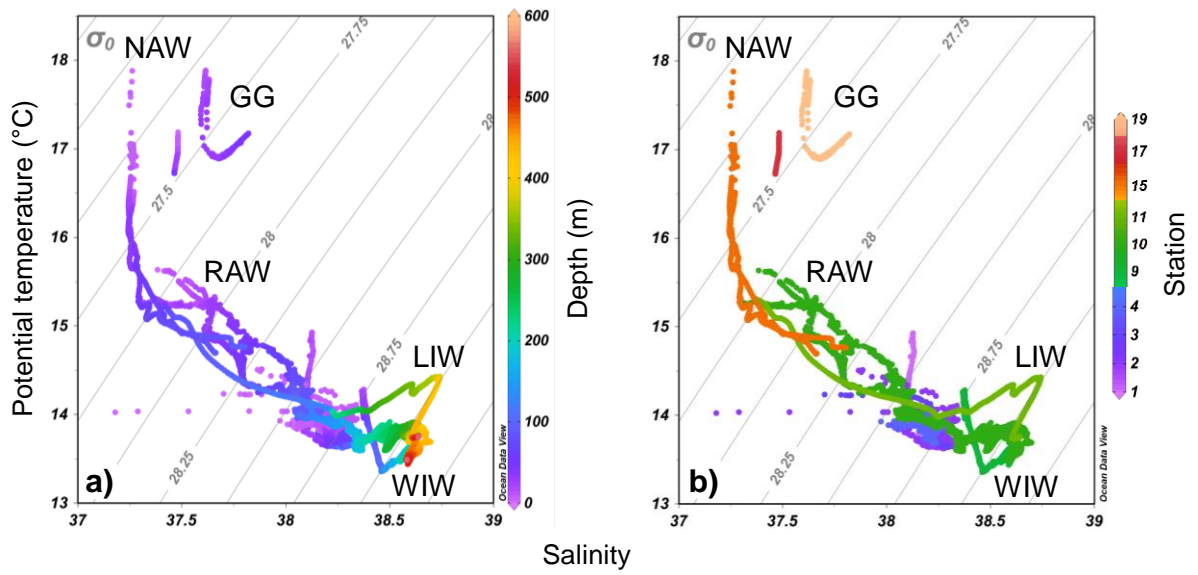


Figure 9

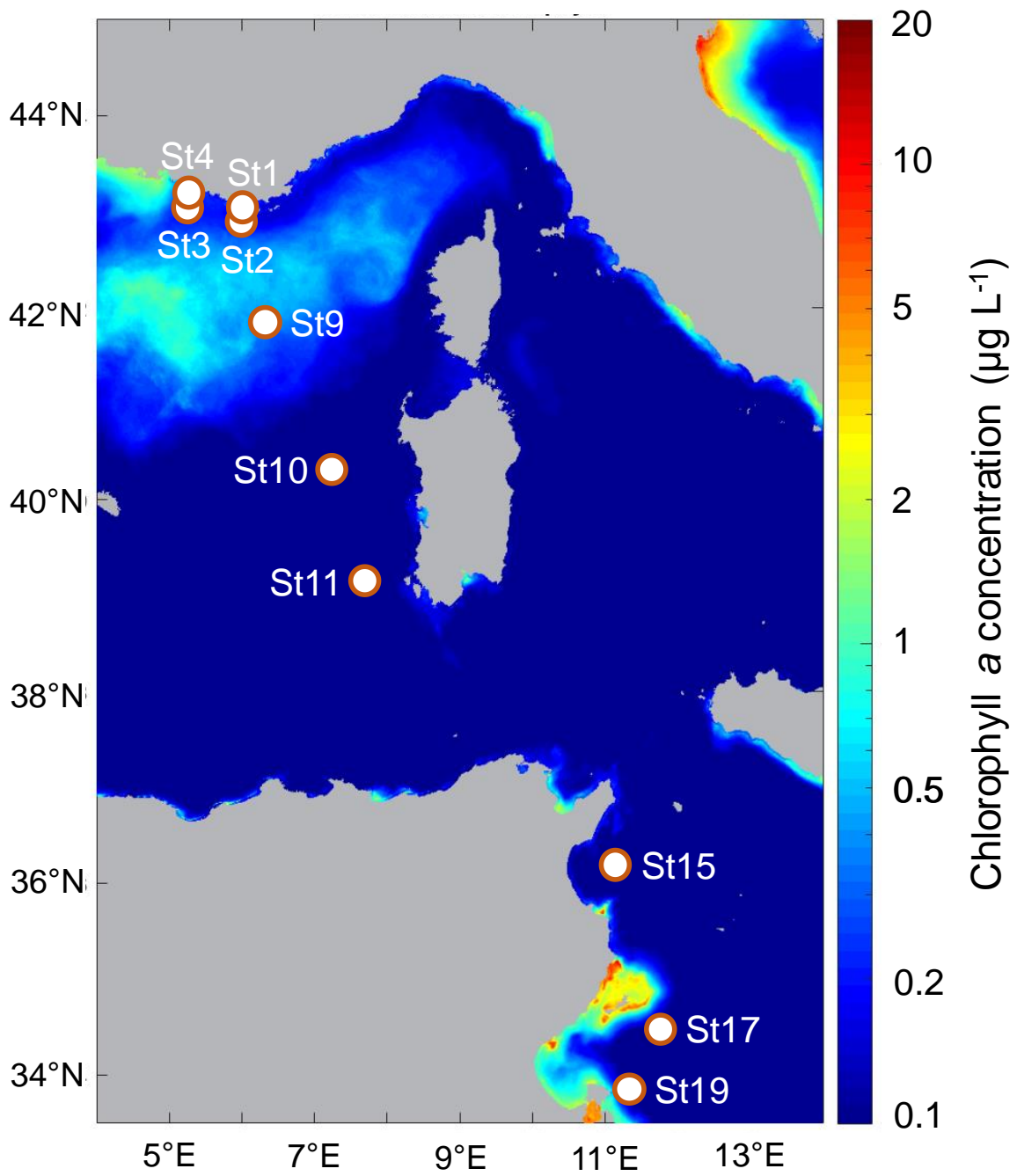


Figure 10

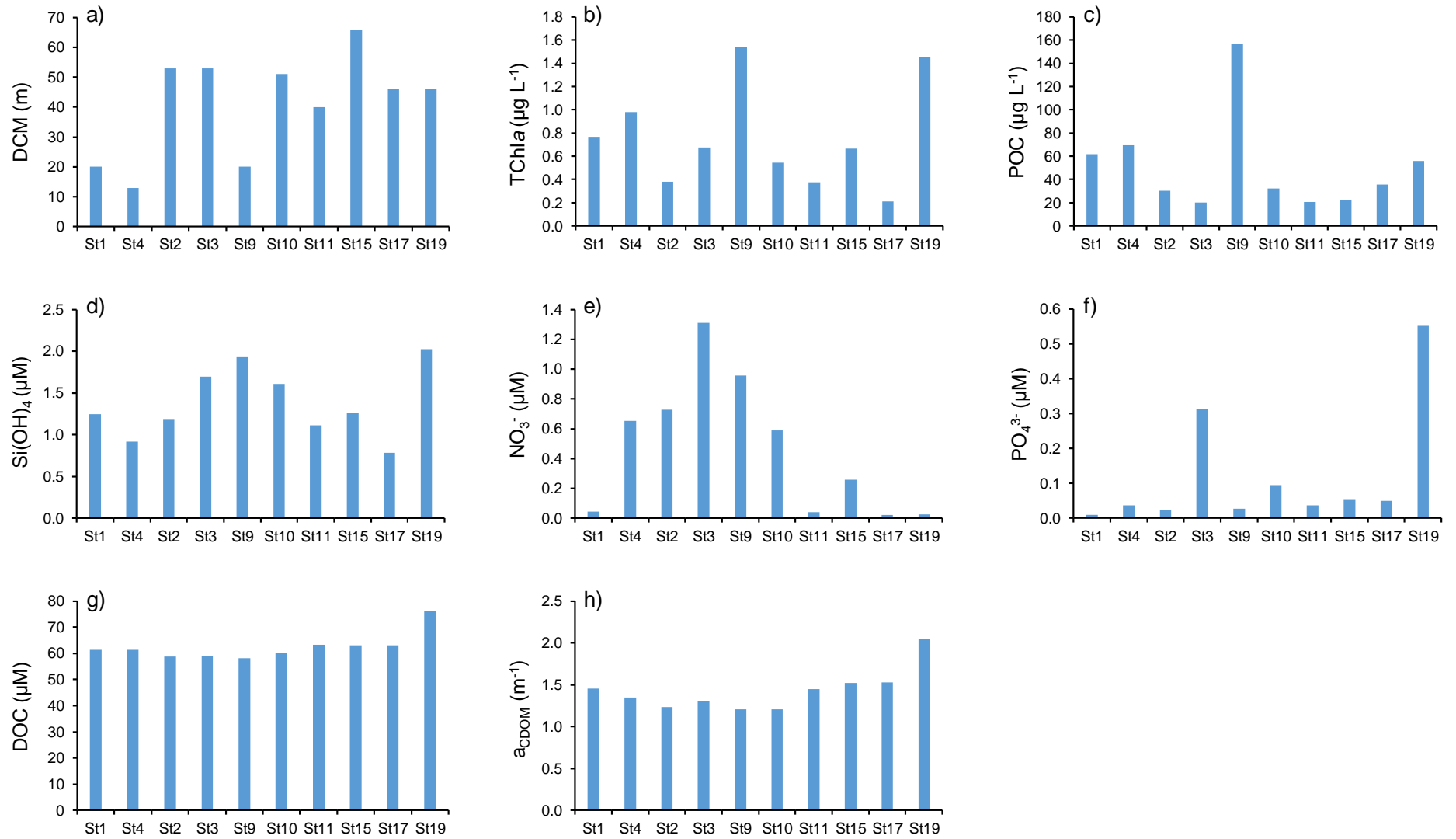


Figure 11



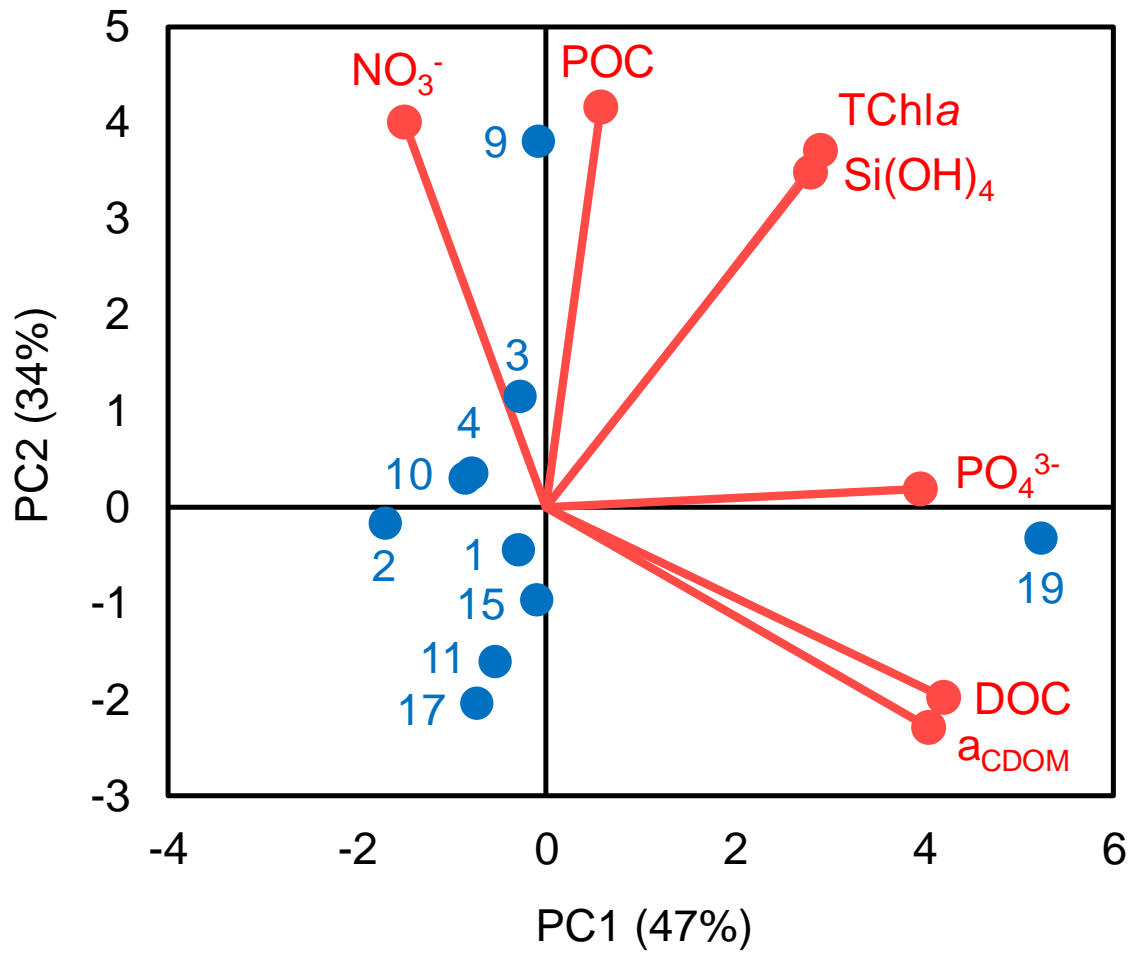


Figure 12

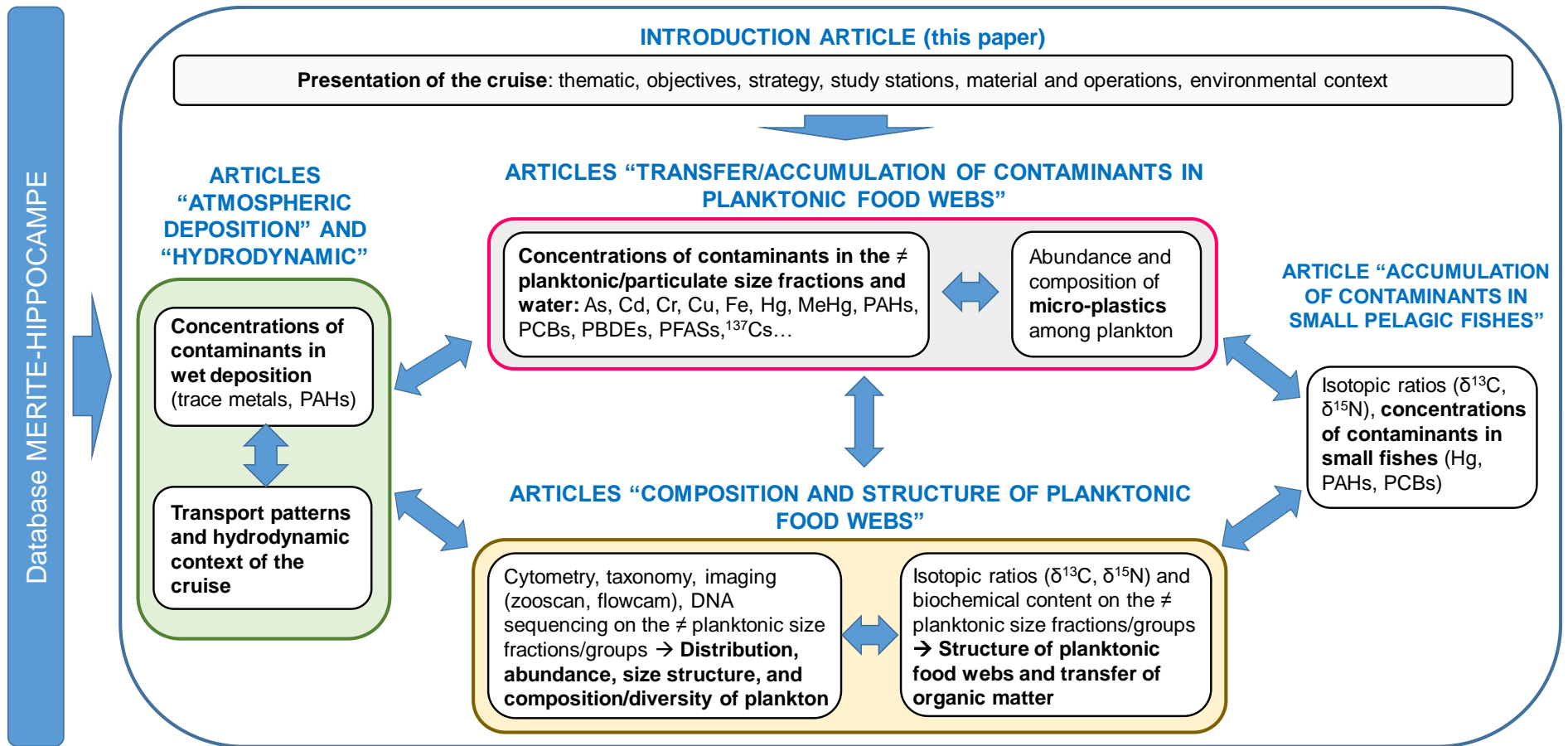


Figure 13

